THE ORIGIN OF TRANSPARENT AND NON-TRANSPARENT WHITE PUMICE: A CASE STUDY OF THE 52 ka MANINJAU CALDERA-FORMING ERUPTION, INDONESIA

インドラノバ, スヘンドロ

九州大学大学院理学府　地球惑星科学専攻

博士論文

THE ORIGIN OF TRANSPARENT AND NON-TRANSPARENT WHITE PUMICE: A CASE STUDY OF THE 52 ka MANINJAU CALDERA-FORMING ERUPTION, INDONESIA

岩石循環科学研究分野

INDRANOVA SUHENDRO

インドラノバ　スヘンドロ

2021 年 8 月

ABSTRACT

The 52 ka eruption of Maninjau caldera in Indonesia produced two distinctive type of white pumices: transparent (TWP) and non-transparent (NTWP). Both pumice types are crystal-poor (avg. 3.3 %), having similar mineralogy, similar glass compositions (avg. 78.5 wt. % SiO_2), and similar plagioclase core compositions (avg. An_{24}). We found that the abundance of TWP decreases towards the upper stratigraphic ignimbrite deposits, together with the increase in NTWP, grey pumice, banded pumice, and lithic (non-juvenile) contents. The TWP are typically dominated by large vesicles, while NTWP characterized by abundant-small vesicles. Large vesicle corresponds to the preexisting vesicle which formed in magma chamber (pheno-vesicle, > 0.1 mm). On the other hand, small vesicle in groundmass (matrix-vesicle, <0.1 mm) is attributed to second nucleation in the conduit during the eruption. We performed quantitative comparison using vesicle data (pheno- and matrix-vesicles) for these two white pumice types. The correlation between pheno- and matrix-vesicles results in negative correlation. We also found that the boundary between TWP and NTWP is clearly defined by the volume fraction and number density ratio of pheno- and matrix-vesicles. Namely TWP originates from phenovesicle-dominated magma, while NTWP dose from phenovesicle-poor magma. In terms of number density, the correlation between pheno-vesicle number density (PVND) and matrix-vesicle number density (MVND) result in two regimes: (1) decompression-controlled regime, showing nearly constant-PVND correlation for TWP, and (2) phenovesicle-controlled regime, showing steeply-decreasing PVND correlation for NTWP. In the first regime, MVNDs value varies dramatically, suggesting the variation of decompression rate by two to three orders of magnitudes. While in the second regime, the slight increase of MVNDs are considered as the effect of the decrease in PVND within the nearly constant decompression rate.

Keywords: Maninjau; transparent white pumice; pheno-vesicle; matrix-vesicle; bimodal vesicle population; vesicle number density

Table of contents (目次)

1. Introduction

Vesicles in pyroclasts are believed to record the physical state and vesiculation history of magma, either in magma chamber and conduit (e.g., Klug and Cashman 1994, 1996; Klug et al. 2002; Gurioli et al. 2005; Toramaru 2006, 2014; Shea et al. 2011; Shea 2017; Edmonds and Woods 2018). Such vesiculation process in magma chamber, which occurs via heterogeneous nucleation in cooling-crystallization (second boiling) is represented by pre-eruptive vesicles and named as pheno-vesicle (Toramaru, 2014) (**Fig. 1A**). On the other hand, the vesiculation in conduit, which occurs as homogeneous nucleation (or often called second nucleation in magmas with pre-eruptive vesicles) under decompression, is recorded by syn-eruptive vesicles and defined as matrix-vesicle (Toramaru, 2014) (**Fig. 1A**). This hypothesis is emphasized by the evidence of bimodal vesicle population of small and large vesicles in the vesicle size distributions (VSDs) plot as reported in the 182 ka eruption of Lower Pumice 1-Santorini, the 7.7 BP eruption of Mazama, the 1.8 ka eruption of Taupo, the 79 AD eruption of Vesuvius, the 1980 AD eruption of St. Helens, and the 2012 AD eruption of Havre (Simmons et al. 2017; Klug et al. 2002; Houghton et al. 2010; Gurioli et al. 2005, Shea et al. 2012; Klug and Cashman 1994, 1996; Mitchell et al. 2019) (**Fig. 1B**). Moreover, the introduction of pheno- and matrix-vesicles thus become essential to advance the understanding of eruption dynamics, not only because pheno-vesicles provides buoyancy and/or overpressure in magma chamber (thus triggers an eruption), but also controls second nucleation under decompression during the eruption. Particularly, high pheno-vesicle number density magmas will limit the second nucleation because supersaturation is effectively diminished by the overgrowth of pheno-vesicles (Toramaru, 2014). Hence, higher magma decompression rate is needed in order to generate second nucleation in high pheno-vesicle number density magmas. By applying this idea to natural samples, it has been demonstrated that pyroclasts from the previously-mentioned eruptions are containing abundant small vesicles with high matrix-vesicle number density values (suggesting that the magma experience with high decompression rate and the number density of pheno-vesicles was not significantly limit the supersaturation of matrix-vesicles during the eruption) and look not transparent (**Fig. 1C**).

Interestingly, we found that the VEI-7 (220-250 km^3 erupted volume) and 52 ka eruption of Maninjau caldera in West Sumatra, Indonesia (Purbo-Hadiwidjoyo et al.1979; Alloway et al. 2004) (**Fig. 2**), produced an unusual white pumice type that we call transparent pumice (TWP), which lacks matrix-vesicle and mainly includes pheno-vesicle, together with the common white pumice type that we call non-transparent pumice (NTWP) that includes dense population of matrix-vesicles and lacks pheno-vesicle (**Fig. 2C, D**). This leaves an important question: what factor controls the formation of TWP and NTWP within the same eruption?

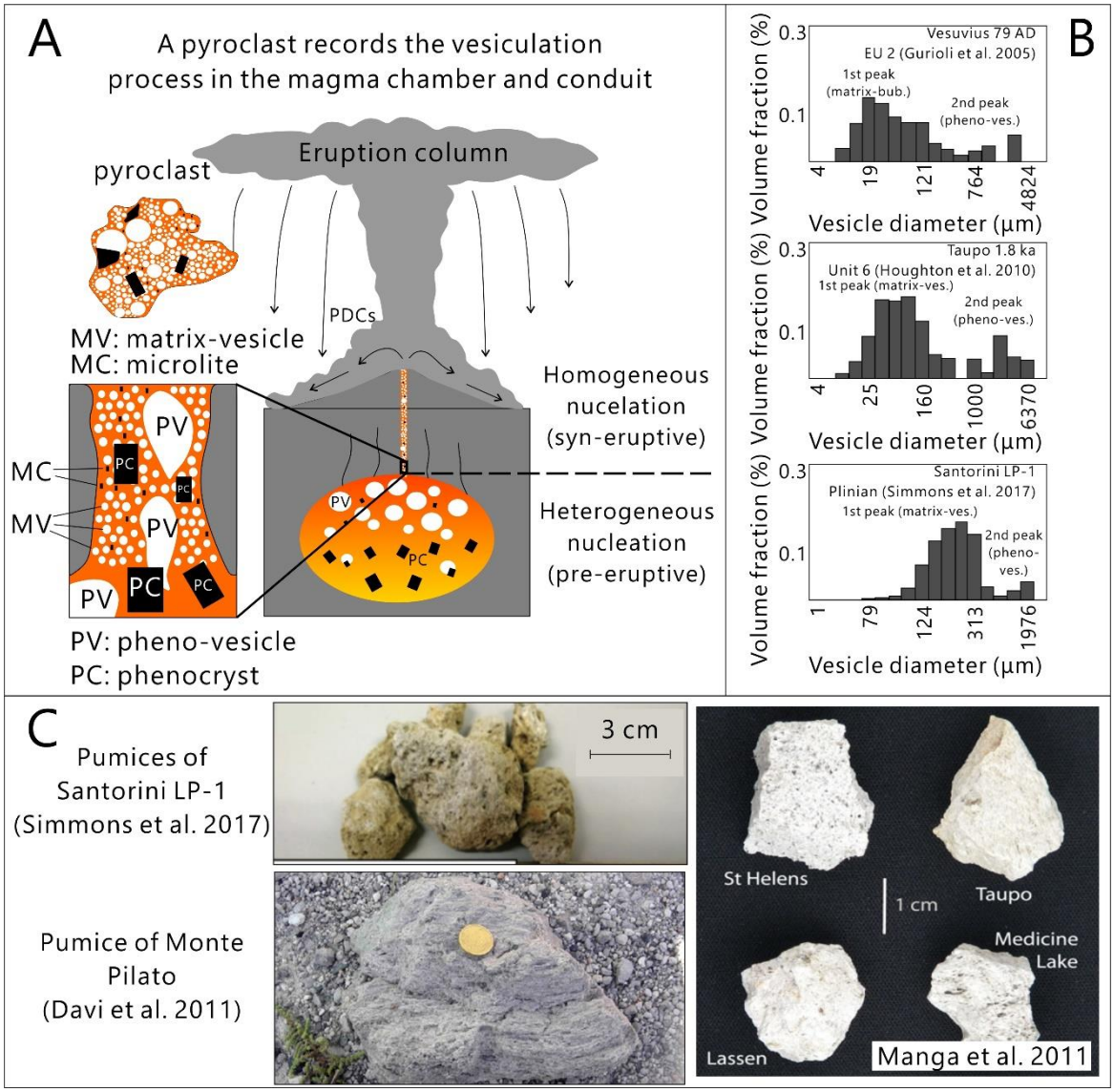

Figure 1. (A) Illustration of magma's vesiculation history, including the pre- and syn-eruptive processes. (B) Some examples of bimodal population of vesicle size distributions (VSDs). Note the difference of x-axes between each sample. (C) Some examples of pumices from explosive eruptions. These pumices are typically abundant in small vesicles (matrix-vesicle) and look not transparent.

In order to elucidate the main issue of this study, first, we explain our detailed stratigraphic data which obtained during fieldwork, corresponding to the 52 ka eruption deposits. Next, we attempted to reconstruct the vertical and lateral variation of the 52 ka ignimbrite deposits by combining the stratigraphy and componentry data. We also identify the magmatic origin of the 52 ka juvenile materials based on petrography and chemical compositions. Finally, we will present the novel interpretation regarding to the formation of TWP and NTWP on the basis data of quantitative comparison between pheno- and matrix-vesicles (e.g., volume fraction and number density). Based on these results, we argue that the transitions

between TWP and NTWP strongly depends on the intensity of matrix-vesicle nucleation that controlled by magma decompression rate and the vertical variation of pheno-vesicle abundance in the pre-eruptive magma chamber.

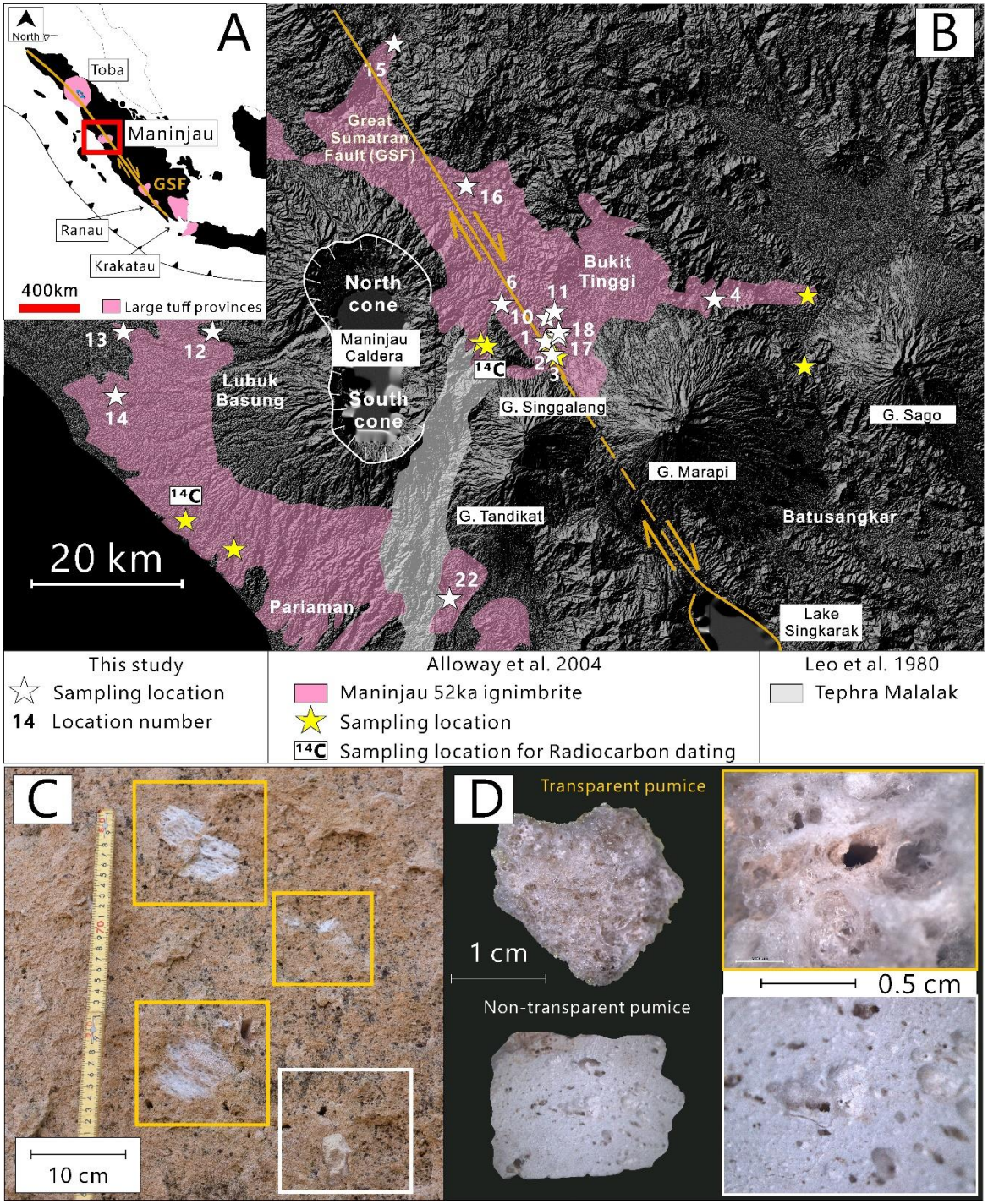

Figure 2. (A) Distribution map of some major caldera forming eruptions in Sumatra Island, Indonesia, modified from Salisbury et al. (2012). Maninjau caldera is highlighted in req square. (B) Sampling locations of this study (white star) and Alloway et al. (2004) (yellow star). (C) Co-existence of transparent (TWP) and non-transparent white (NTWP) pumice at the same deposit. Yellow square and white square denotes TWP and NTWP, respectively. (D) Detailed megascopic image of TWP and NTWP.

2. Maninjau caldera, Indonesia

Maninjau caldera is one of the largest calderas in Indonesia (220-250 km^3 erupted volume; Purbo-Hadiwidjoyo et al. 1979) that is situated in Sumatra Island, above the subduction zone between Eurasian and Indo-Australian plates (**Fig. 2A**). Alloway et al. (2004) described that the lowermost ignimbrite is characterized by the numerous stratifications of a thin-pyroclastic density current units (PDCs) that rich in gas pipe structures. Further upward, the ignimbrite shifted to thick and massive facies without any occurrence of stratification and gas pipe structures. The eruption age 52 ±3 ka was obtained from ^{14}C dating for southwestern and eastern ignimbrite deposits (Alloway et al. 2004) (**Fig. 2B**). Some previous and more recent studies have shown that Maninjau pre-caldera lavas span from basaltic andesite to andesite (whole rock; 55 – 60 wt. % SiO_2), while the 52 ka ignimbrite is rhyolitic in composition (whole rock; 74 – 77 wt. % SiO_2) (Harahap and Abidin, 2006; Leo et al. 1980; de Maisonneuve and Bergal-Kulvikas, 2020).

3. Fieldwork and stratigraphy

We established eighteen observation locations, including the north-, west-, south-, and east deposits in order to identify and reconstruct the vertical and lateral variations of the deposits (**Fig. 2B**). We observed that the Maninjau caldera-forming eruption deposits include a thick succession (up to 200 m) of dominantly-massive ignimbrite without any precursory fall deposits (Plinian-free eruption). Although the Maninjau ignimbrite is radially distributed to all directions, the most complete stratigraphic succession only can be observed in the eastern deposits, particularly at a deeply-incised valley named 'Ngarai Sianok' (**Fig. 3A**). Here, we were able to observe the whole sequence of the Maninjau ignimbrite, starting from the bottom (690 m elevation) that mainly includes a stratified ignimbrite, to the top of the valley (900 m elevation) that displays a typically massive ignimbrite (**Fig. 3C**). However, the condition of dense vegetation in this vicinity limits our purpose to document the whole-vertical variation of the deposits, thus results in some vertical gaps (blank zone) in the stratigraphy data (**Fig. 4**).

The ignimbrite deposit at the bottom of Ngarai Sianok (represents by LOC 1, 2, and 3; 690-720 m elevation) is characterized by the intercalation of numerous thin-PDC (pyroclastic density current) layers (**Fig. 4**). These thin-PDC layers can be recognized into four different types as lithic-concentrated layer (LCL), pumice-concentrated layer (PCL), massive layer (ML), and fine ash layer (FAL) (**Fig. 4**). Here, pumice fragments vary from 0.2 to 10 cm in size. Most of the large pumice fragments are preserved within the PCL, whereas most of the smaller pumice fragments are included in the ML and LCL. Lithic fragments are relatively small compared to the pumice size, where the maximum size of observed

lithic fragments only exceed 2 cm. Going upward (represents by LOC 4, 10, 11, 17, and 18; 750-875 m elevation), the ignimbrite suddenly shifted into massive facies, having an abundant pumice fragments, lacks gas pipe structure, and relatively lithic poor (**Fig. 4**). Most of the pumice fragments vary between 0.2 to 10 cm in size, but it can reach up to 30 cm. No lithic fragments exceed more than 2 cm in size. Finally, the highest position of the eastern ignimbrite is observed at LOC 6 (elevation 975 m) and might correspond to the uppermost stratigraphic level of the 52 ka deposits (**Figs. 3C and 4**). Although the ignimbrite display massive structure, it can be clearly distinguished from the massive ignimbrite that we observed at the lower positions (750-875 m) because of the abundant lithic, and grey and banded pumice fragments. Here, the pumice fragments vary from 0.2 to 15 cm and the lithic might exceed 6 cm in size.

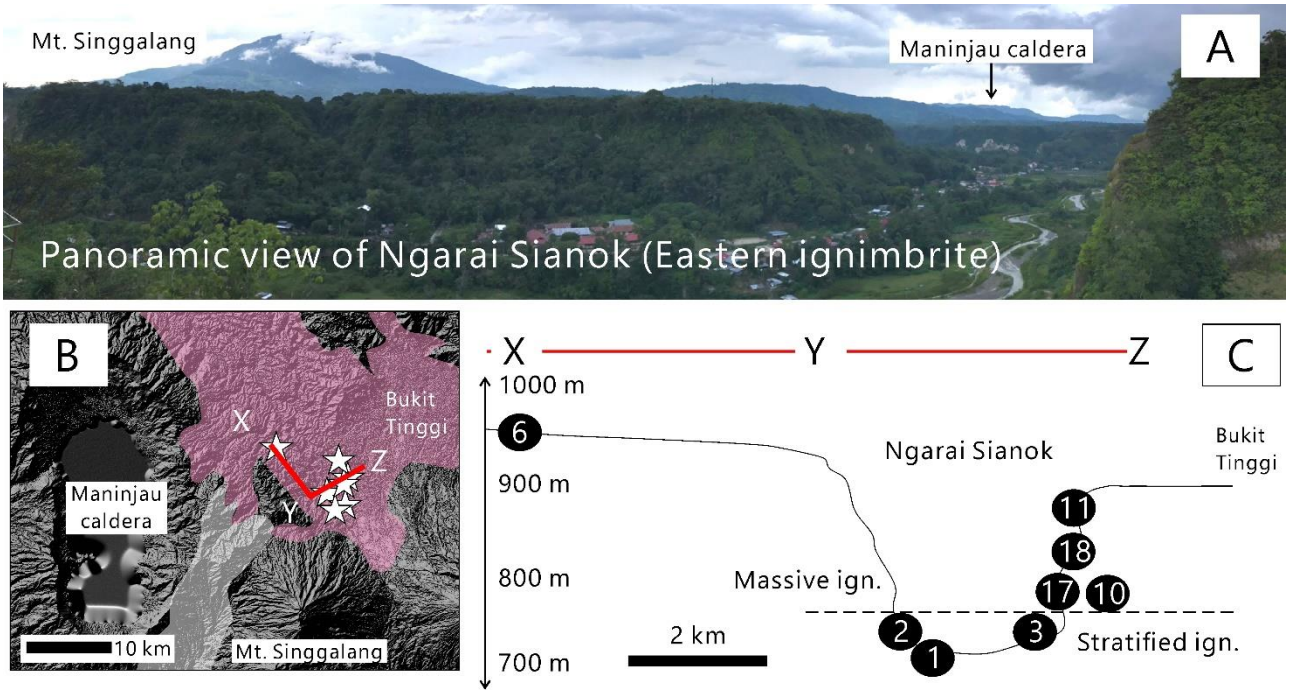

Figure 3. (A) Panoramic view of Ngarai Sianok. (B and C) 2D-Cross sectional view of Ngarai Sianok, including the sampling locations of this study.

By contrast, the ignimbrite in the other directions (north, west, and south) are characterized by a single-flow unit (massive) and does not preserve such thick and various types of deposit. The northern ignimbrite deposits (LOC 15 and 16) seems to have similar appearance to the ignimbrite deposits at LOC 4, 10, 11, 17, and 18 (**Fig. 5**) because it is massive, rich in pumice fragments, lacks gas pipe structure, and relatively lithic poor. No pumice larger than 3 cm was observed at LOC 15. Conversely, at LOC 16, some pumice fragments exceed 10 cm in size. Worthy to note, both locations display the basal contact between the 52 ka ignimbrite and the sedimentary rocks, suggesting the absence of precursory fall deposits (**Fig. 5**). The western (LOC 12, 13, and 14) and southern (LOC 22) display similar characteristics and seems to

be identical with the ignimbrite deposit at LOC 6 (**Fig. 5**) because they are typically massive, having an abundant grey and banded pumice fragments, and is extremely lithic rich. The observed pumice and lithic fragments are typically less than 20 and 10 cm in size, respectively.

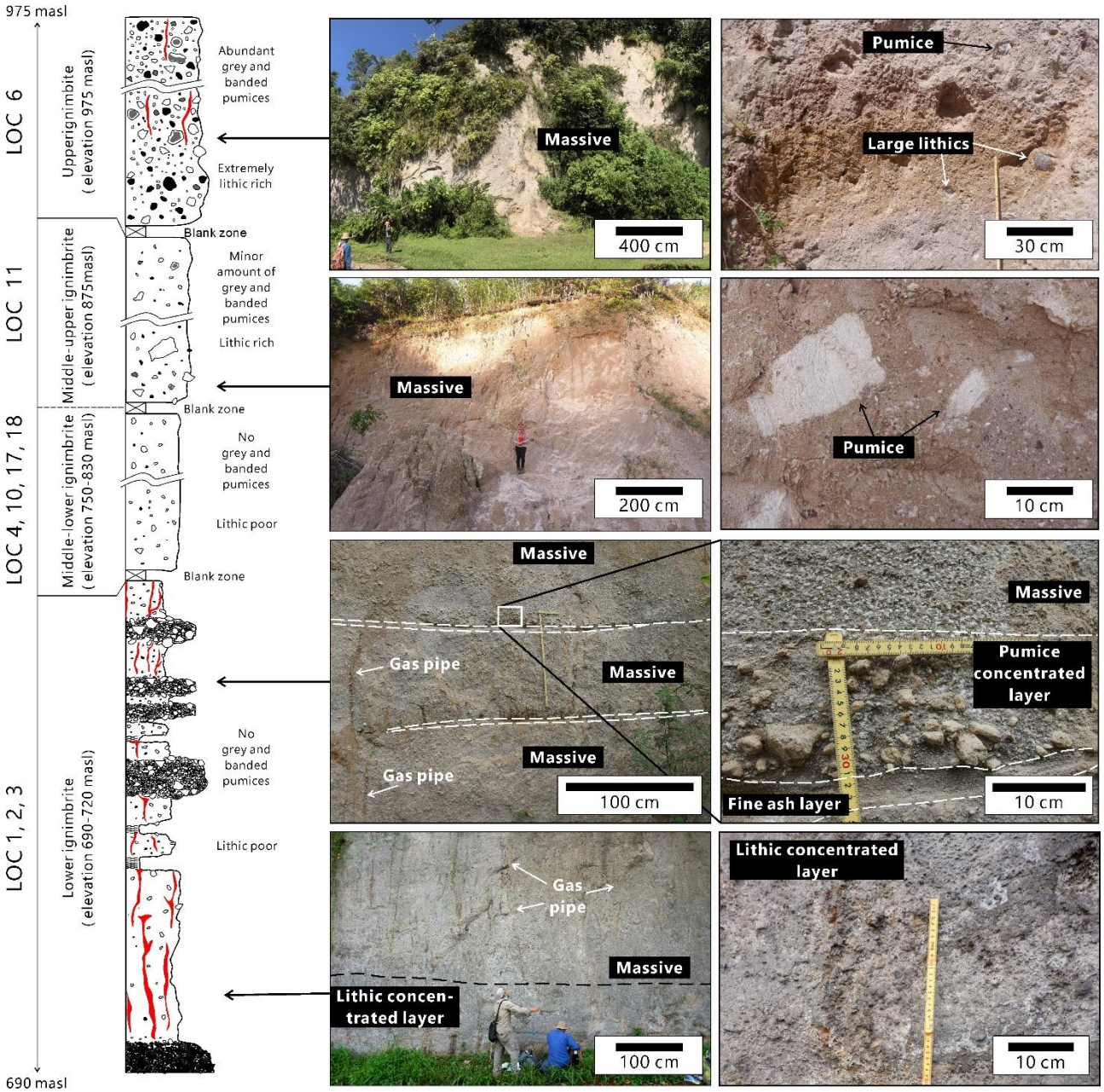

Figure 4. Stratigraphic section and the outcrop images of the eastern ignimbrite deposits. LCL = lithic concentrated layer, PCL = Pumice concentrated layer, ML = Massive layer, and FAL = Fine ash layer. Red color in stratigraphy represents gas pipe structure.

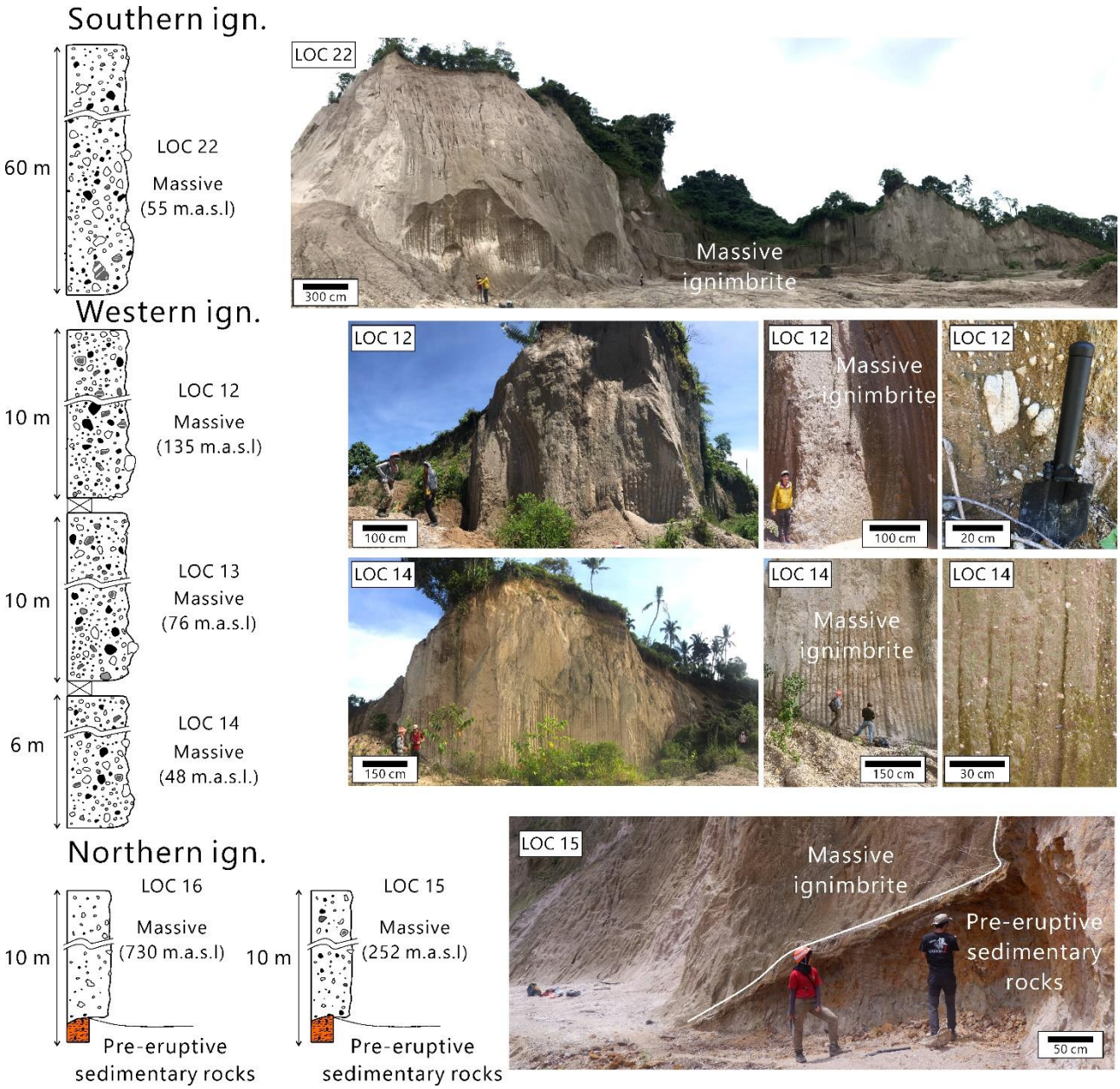

Figure 5. Stratigraphic section and outcrop images of the southern, western, and northern ignimbrite deposits. All of the deposits are typically massive. The basal contact between the Maninjau ignimbrite and paleosoil of pre-eruptive sedimentary rocks was observed at LOC 15 and 16.

4. Analytical methods

4.1. Grain size distribution and componentry

The collected samples were sieved using -5φ (>32 mm) to 1φ (<1/2 mm) sieves in order to obtain the grain size distribution. Next, we qualitatively observe and quantitatively count the whole grains from -5φ (>32 mm) to -1φ (2-4 mm) mesh size in order to identify the main component types.

4.2. Bulk density

We selected 1094 white pumice grains (713 for TWP and 381 for NTWP) within the size of 4 -16 mm. First, we measure the weight using electronic mass balancer. Afterwards, pumice grains were scanned by MEDIT-3D Laser scanner (manufactured by Sea Force Company) and processed by HIRA 3D view software at the Petrology and Volcanology Laboratory, Kyushu University in order to get the 3D surface image and bulk volume of pumice grain. Finally, bulk density can be obtained from simple equation as follow:

$$\rho = m/v \quad (1)$$

where ρ is bulk density in gr/cm^3, m is mass of the grain in gram (gr), and v is volume of the grain in cm^3.

4.3. Petrography, glass, and plagioclase chemical compositions

Thin sections were made by selecting white pumice grains that vary from 4 to 16 mm in size, including the lowest to the highest bulk density value. Samples containing elongated vesicle were cut perpendicular to the elongation direction. Mosaic images for each thin section were taken by using HITACHI TN3030 Plus Miniscope Scanning Electron Microscope (SEM) at the Petrology and Volcanology Laboratory, Kyushu University. Major elements in glass and plagioclase phenocrysts were analyzed by utilizing JEOL JXA 8530-F Field Emission Electron Microprobe at the Faculty of Science, Kyushu University, using a focused beam with 1μm diameter size and 15 kV accelerating voltage.

4.4. Geothermobarometry

The amphibole geothermobarometry formula (equation 1 to 3) was introduced and developed by Ridolfi et al. (2010) by examining the chemical compositions of the amphibole phenocrysts from subduction-related volcanoes with calc-alkaline magma affinity (number = 38) and its relationship with the whole-rock and glass chemical compositions. They found that the aluminum content (in the amphibole) has strong negative correlation with silica, where higher aluminum amphibole dose from a less-evolved magmatic origin and *vice versa* (see **Fig. 1b**, Ridolfi et al. 2010). Since magmatic differentiation is a function of silica (and also the other major oxides), the amphibole compositions can be used as a proxy to estimate the temperature, water, and pressure. The temperature can be obtained by the following equation:

$$T = -151.487Si^{*} + 2.041 \quad (1)$$

where $Si^{*} = Si + \frac{(4)Al}{15} - 2^{(4)}Ti - \frac{(6)Al}{2} - \frac{(6)Ti}{1.8} + \frac{Fe^{3+}}{9} + \frac{Fe^{2+}}{3.3} + \frac{Mg}{26} + \frac{B_{Ca}}{5} + \frac{B_{Na}}{1.3} - \frac{A_{Na}}{15} + \frac{A_{()}}{2.3}$.

While water content and pressure can be obtained from the following equations:

$$H_2O_{melt} = 5.215^{(6)}Al^{*} + 12.28 \quad (2)$$

$$P = 19.209e^{(1.438Al_T)}, R^2 = 0.99 \quad (3)$$

where $^{(6)}Al^{*} = {}^{(6)}Al + \frac{(4)Al}{13.9} - \frac{Si+(6)Ti}{5} - \frac{C_{Fe^{3+}}}{3} - \frac{Mg}{1.7} + \frac{B_{Ca+A_{(\ )}}}{1.2} + \frac{A_{Na}}{2.7} - 1.56K - \frac{Fe\#}{1.6}$.

In this study, about 50 amphibole minerals from grey pumice types (dark grey, pale grey, light grey) were selected for the estimation of temperature, pressure, and water content by using the methods of Ridolfi et al. (2010). The uncertainty for pressure estimation vary from 17-25 MPa and constant for temperature and water content, particularly at 22°C and 0.4 wt.%, respectively. However, we could not perform such methods on white pumice due to the absence of amphibole.

4.5. Quantifying vesicle texture

Three magnifications (mosaic, 200x, and 1200x) of BSE image from each pumice grain were chosen as it is capable to identify the largest and smallest size of pheno- and matrix-vesicles (**Fig. 6**). Bubble coalescences occur in all vesicle size, more or less. Therefore, correcting each vesicle morphologies from coalescence process is highly important in order to represent the actual distribution value of the vesicle size, before the coalescence occur. The interconnected vesicles were manually separated (decoalesced), following the method of Klug and Cashman (1994, 1996). Finally, the digitized images were processed by using Image-J software to obtain the area of vesicle. The results were plotted as volume fraction curves, forming 2D-vesicle size distribution (VSD). Both white pumice types show bimodal distribution of VSDs, where the decay of each population are terminated at the beginning of second peak around 0.1 mm vesicle diameter. Therefore, the pheno-vesicle number density (PVND) and matrix-vesicle number density (MVND) were only determined for vesicle sizes larger than 0.1 mm and smaller than 0.1 mm, respectively. The PVND and MVND values were corrected by bulk- and matrix-vesicle vesicularities as follows:

$$PVND\ (N_{pv}) = (N_{ap}/d_p) * (1/1 - \varphi_{bv}) \quad (4)$$

$$MVND\ (N_{mv}) = (N_{am}/d_m) * (1/1 - \varphi_{mv}) \quad (5)$$

where N_{ap} is number density per unit area of pheno-vesicle, d_p is the average pheno-vesicle size, φ_{bv} is bulk vesicularity, N_{am} is number density per unit area of matrix-vesicle, and d_m is the average matrix-vesicle size, φ_{mv} is groundmass or matrix vesicularity.

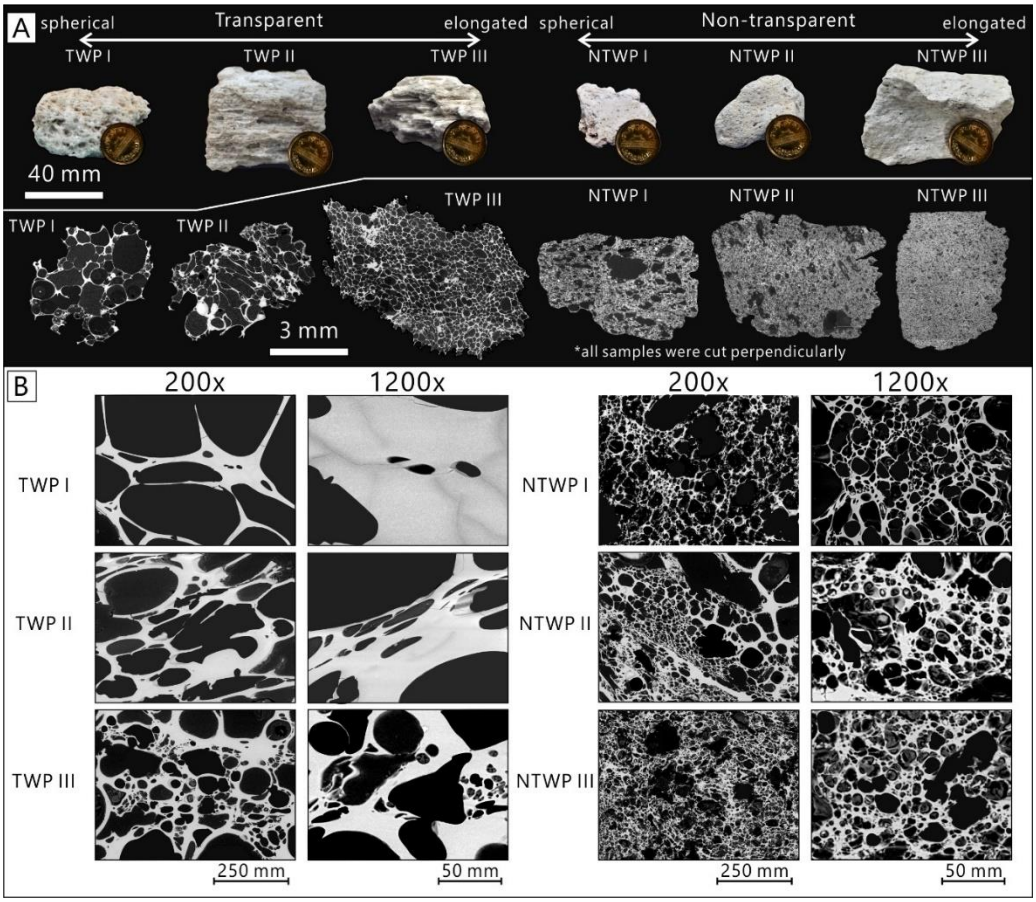

Figure 6. (A) Macroscopic and BSE mosaic images of TWP and NTWP with respect to its vesicle morphologies. (B) Characteristic vesicle textures of TWP and NTWP. From left to right, each image denotes 200x and 1200x image magnifications. From top to bottom, each image denotes type I, II, and III.

5. Results

5.1. Component variations

We found that Maninjau ignimbrite consists of five main components as white pumice, grey pumice, banded pumice, lithic, and crystal. White pumice can be classified into transparent (TWP) and non-transparent (NTWP) type. TWP is typically glass-like, dominated in large vesicles, having irregular grain shape, and fragile. Conversely, NTWP is apparently non-glassy, lack of large vesicles, blocky in grain shape, and hard (**Fig. 6A**). Furthermore, each white pumice type can be sub-classified into three sub-classes based on the vesicle morphologies. Type I mainly includes spherical

vesicles, type II is a combination of spherical and elongated vesicles, and type III mainly includes elongated vesicles (Fig. 5A). All sub-classifications of TWP distribute in the whole ignimbrite directions by following proportion: III (29 %) > II (19 %) > I (9 %). In contrast, most of NTWP correspond to type III (40 %). NTWP-I and II are absent in eastern deposits and their abundance are relatively rare (1 % and 2 %, respectively). In total, transparent type is the dominant phase of white pumice. Particularly, TWP exceeds 57 %, more than half portion of white pumice, while NTWP comprise 43 %.

Based on color variation, grey pumice can be divided to dark grey and pale grey (**Fig. 7**). Interestingly, we found the other grey color in terms of banded pumice that observed as light grey (**Fig. 8**). All grey pumice types are apparently crystal-rich and have abundant mafic mineral content.

Lithic (non-juvenile) fragments can be divided to volcanic and basement lithics (**Fig. 9**). Volcanic lithic is the main phase of the lithic content (mostly > 95 % portion of lithic) and mostly correspond to a crystal-rich lava that display porphyritic texture. By contrast, basement lithic is considerably minor (mostly <5 % portion of lithic) and it comprise quartzite and metasedimentary rocks. Free crystal mostly consists of plagioclase and quartz with negligible amount of mafic minerals such as biotite and pyroxene (**Fig. 9**). However, in this study, we combined all crystal types and define them as free crystals.

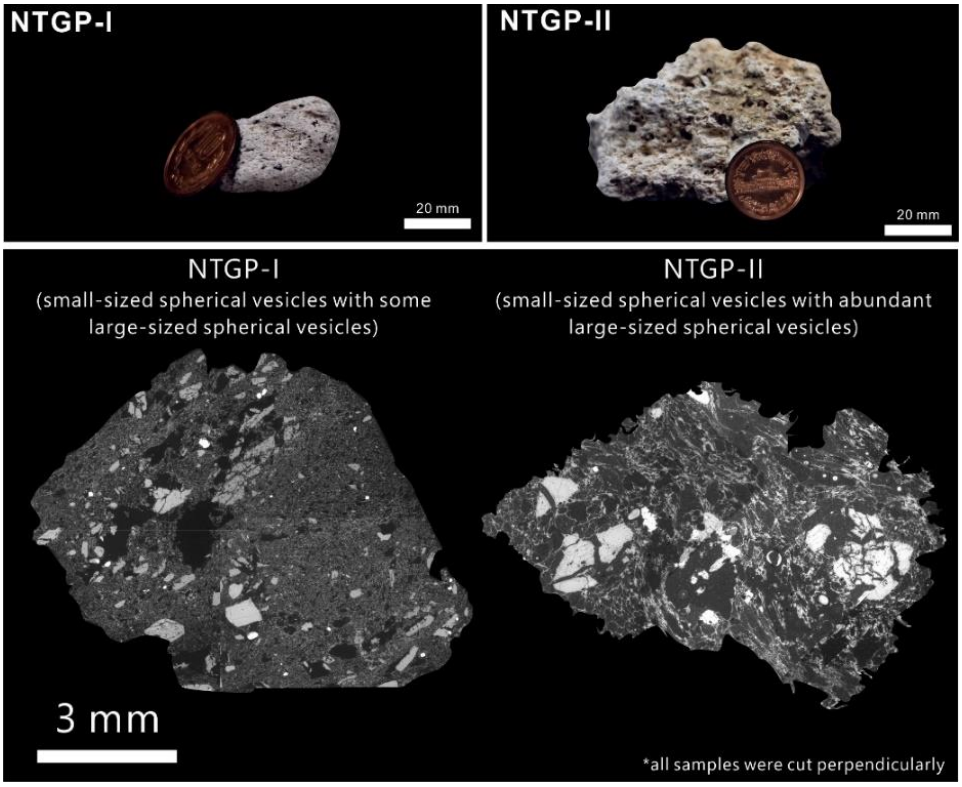

Figure 7. Grain and BSE mosaic images of dark grey and pale grey pumices of the Maninjau 52 ka eruption.

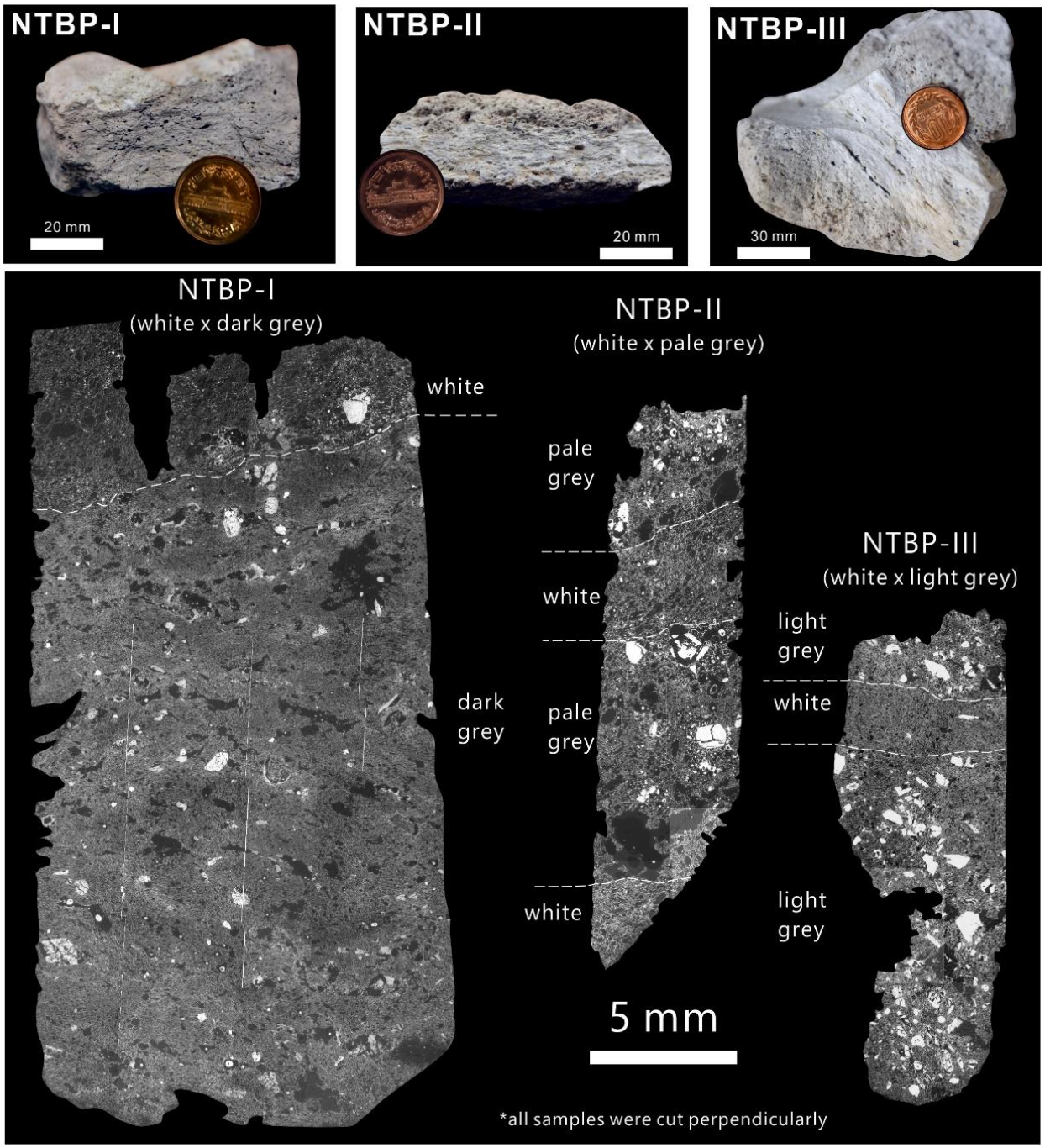

Figure 8. Grain and BSE mosaic images of banded pumices of the 52 ka Maninjau eruption. Banding between white and dark grey pumice, white and pale grey pumice, and white and light grey pumice are represents as NTBP-1, NTPBP-2, and NTBP-3, respectively.

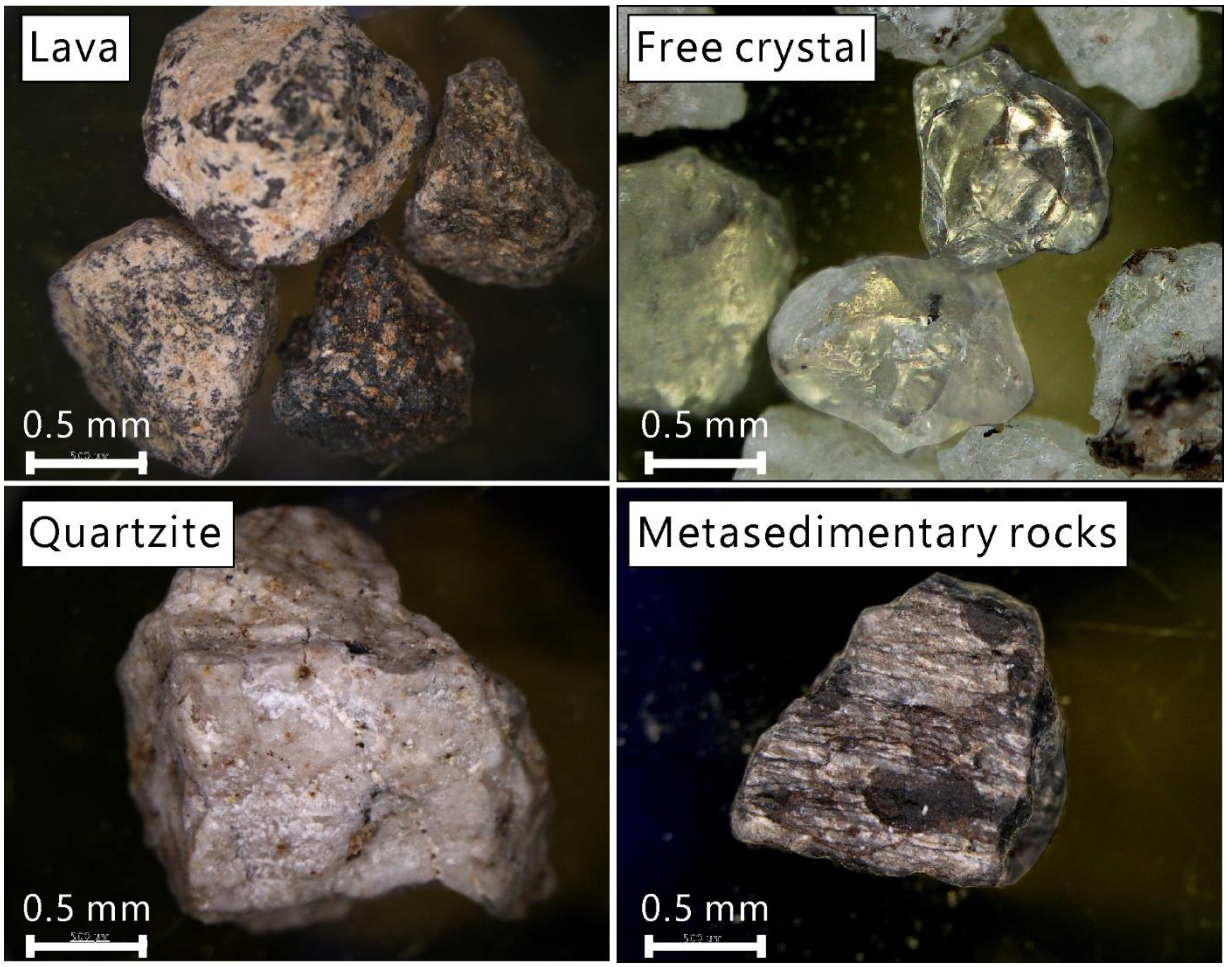

Figure 9. Grain images of volcanic lithic (lava) and metamorphic lithic (quartzite and metasedimentary rocks), and free crystal.

5.2. Vertical and lateral variation of the 52 ka Maninjau ignimbrite inferred from componentry

First, we assume that the eastern ignimbrite deposits represent the most 'complete' stratigraphic section of the 52 ka eruption deposits. Therefore, the vertical variation of componentry data from the eastern ignimbrite deposit can be used as a backbone to make lateral stratigraphic correlation with the other deposits in the other directions (**Fig. 10A**). Based on the facies and componentry data, we define the stratigraphy into three units as unit A, B, and C (**Fig. 10**).

5.2.1. Vertical variation

The first unit (unit A) correspond to the stratified ignimbrite which is situated at bottom of Ngarai Sianok (LOC 1, 2, and 3; 690 – 720 m elevation) (Fig. 6). Here, the PCL (pumice-concentrated layer) and ML (massive layer) facies are dominated in TWP (73 – 77 %), having low abundance of NTWP (21 – 25 %) and lithic (3 – 4 %) content, except for the LCL (lithic-concentrated layer) facies which is dominantly consist of lithic (22 % TWP, 8 % NTWP, and 70 % lithic).

Most of the lithic fragments in LCL, PCL, and ML facies correspond to volcanic lithics, whereas basement lithics are subordinate (average of <0.1 %) (**Fig. 10B**).

The second unit (unit B) correspond to the massive ignimbrite that situated above the stratified ignimbrite (LOC 10, 11, 17, and 18; elevation 750 – 875 m) (**Fig. 10**). Here, the TWP is still dominating the componentry and its proportion is relatively higher compared to the unit A (78 – 87 %). We found that the unit B deposits preserves relatively higher lithic content than unit A (except for LCL) as it vary from 4 to 9 %. Moreover, the increment of lithic is also accompanied by the slight increase in basement lithics, as it reach up to 0.3 % (**Fig. 10B**). Note that the grey-banded pumice is only observed at the LOC 11, which correspond to the highest elevation among all locations of the unit B. We ought that the occurrence of grey and banded pumice might be important for reconstructing the eruption chronology. Therefore, on the basis of the existence of grey and banded pumice, we tend to divide the unit B into two sub-units (B-1 and B-2) (**Fig. 10**).

The last unit (unit C) correspond to the massive ignimbrite that positioned in the highest elevation around the vicinity of Ngarai Sianok (LOC 6; 975 m elevation) (**Fig. 10**). As opposed to unit A and B, this unit is characterized by the domination of NTWP (34 % NTWP and 27 % TWP) and include an extremely abundant proportion of grey-banded pumice and lithic content (14 % for GP+BP and 24 % for lithic). Worthy to note, the basement lithics reached 4 % of total componentry, making this unit is extremely rich in basement rocks relative to the other units. Therefore, it can be simply inferred that the abundance of TWP is decreasing from the lower towards the upper stratigraphic position (unit A to C), and it is accompanied with the increase of NTWP, grey-banded pumice, and lithic content.

5.2.2. Lateral variation

Our componentry data indicates that the northern deposits (LOC 15 and 16) seems to be equivalent to the unit B-2 of eastern ignimbrite deposits due to the occurrence of grey and banded pumice, in addition to the abundant transparent type and moderate lithic content. Here, the portion of basement lithic is considerably higher than the eastern deposits, particularly 1 % for LOC 15 and 0.4 % for LOC 16.

The western (LOC 12, 13, and 14) and southern ignimbrite deposits (LOC 22) have very similar characteristics in terms of appearance and componentry data to the unit C (**Fig. 10**). Particularly, the ignimbrite is dominated in NTWP (45 – 57 % of NTWP and 6 – 24 % of TWP) and consisting of abundant grey-banded pumice (6 – 24 %) and lithic (18 – 25 %) contents. Although western and southern ignimbrite deposits preserves less proportion of basement lithics than LOC 6, its abundance (0.7 – 1 %) is still considerably high compared to unit A and B (except for LOC 15).

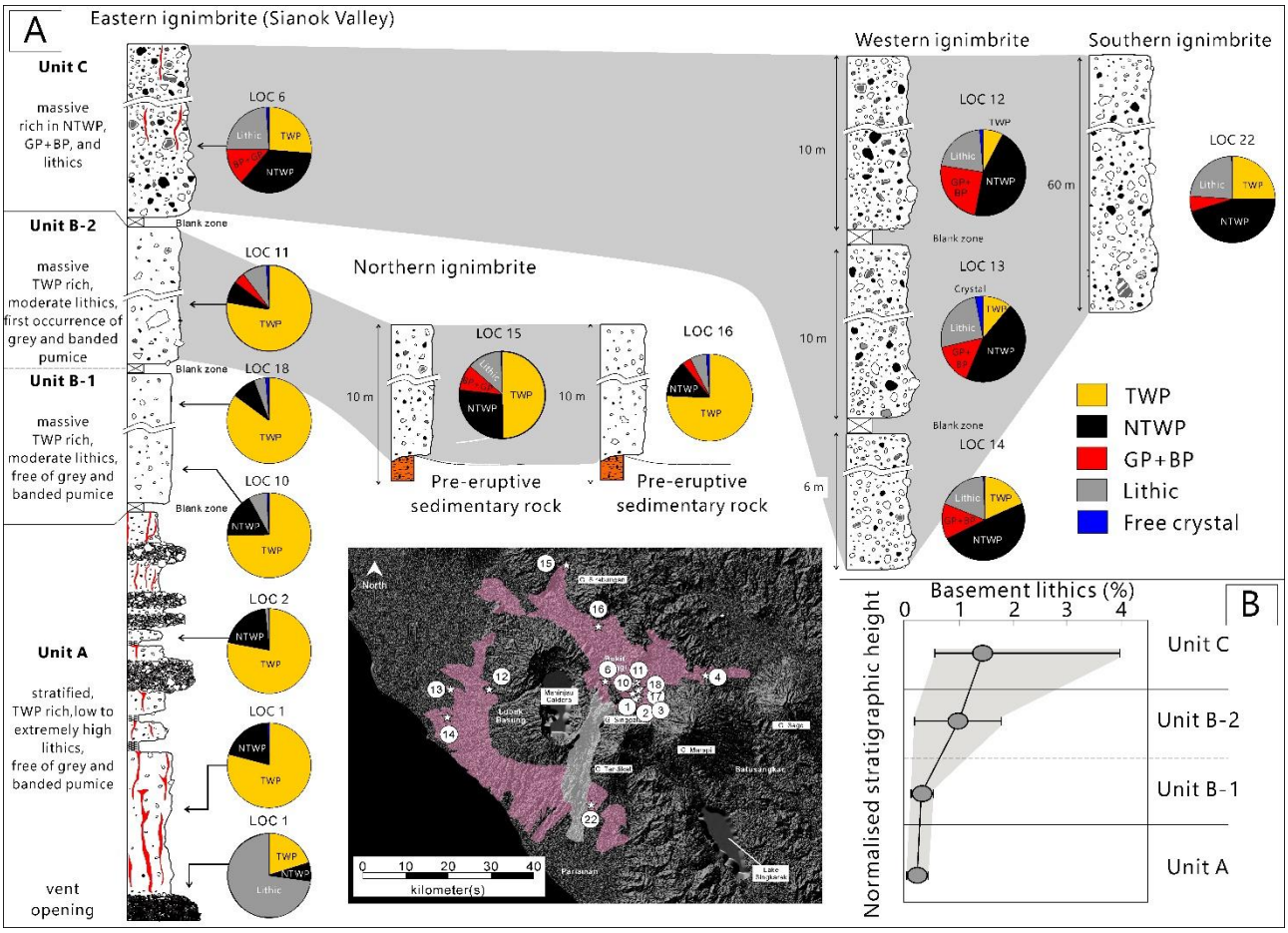

Figure 10. (A) Stratigraphy correlation inferred from componentry data. Pie charts correspond to the componentry variation. Yellow = transparent white pumice, black = non-transparent white pumice, red = grey and banded pumice, grey = lithics (volcanic + metamorphic), blue = free crystal. (B) Variation of basement lithic contents (quartzite + metasedimentary rocks) from unit A to C.

5.3. Grain size distribution

All ignimbrite deposits are plotted within the region of pyroclastic flow (Walker 1976) (**Fig.11A)**, having dominantly bimodal distribution of the grain size (except for LOC 4 and 15) (**Fig. 11B**), and notably, there is tendency for grain size to increase when the deposits contain higher amount of non-transparent white pumice and *vice versa* (**Fig. 11A**).

5.4. Density variation

TWP has slightly higher average bulk density value compared to NTWP (0.67 gr/cm^3 for TWP and average 0.61 gr/cm^3 for NTWP) (**Fig. 11**). There is tendency for bulk density to increase from type I to III. Particularly, the average

bulk density vary from 0.51, 0.63, and 0.80 gr/cm^3 for TWP, and 0.34, 0.68, 0.79 gr/cm^3 for NTWP with respective vesicle types. Dark grey and pale grey pumice has the highest and lowest average bulk density value among all pumice types, as its average density values comprise 0.74 gr/cm^3 and 0.47 gr/cm^3, respectively (**Fig. 12**). Such bulk density measurement cannot be performed on light grey pumice because it only occur as banded phase. In this case, we found that bulk density is strongly controlled by the bulk vesicularity (i.e., lower density pumice results via higher vesicularity and *vice versa*) and it has no correlation with phenocryst content (**Fig. 13**).

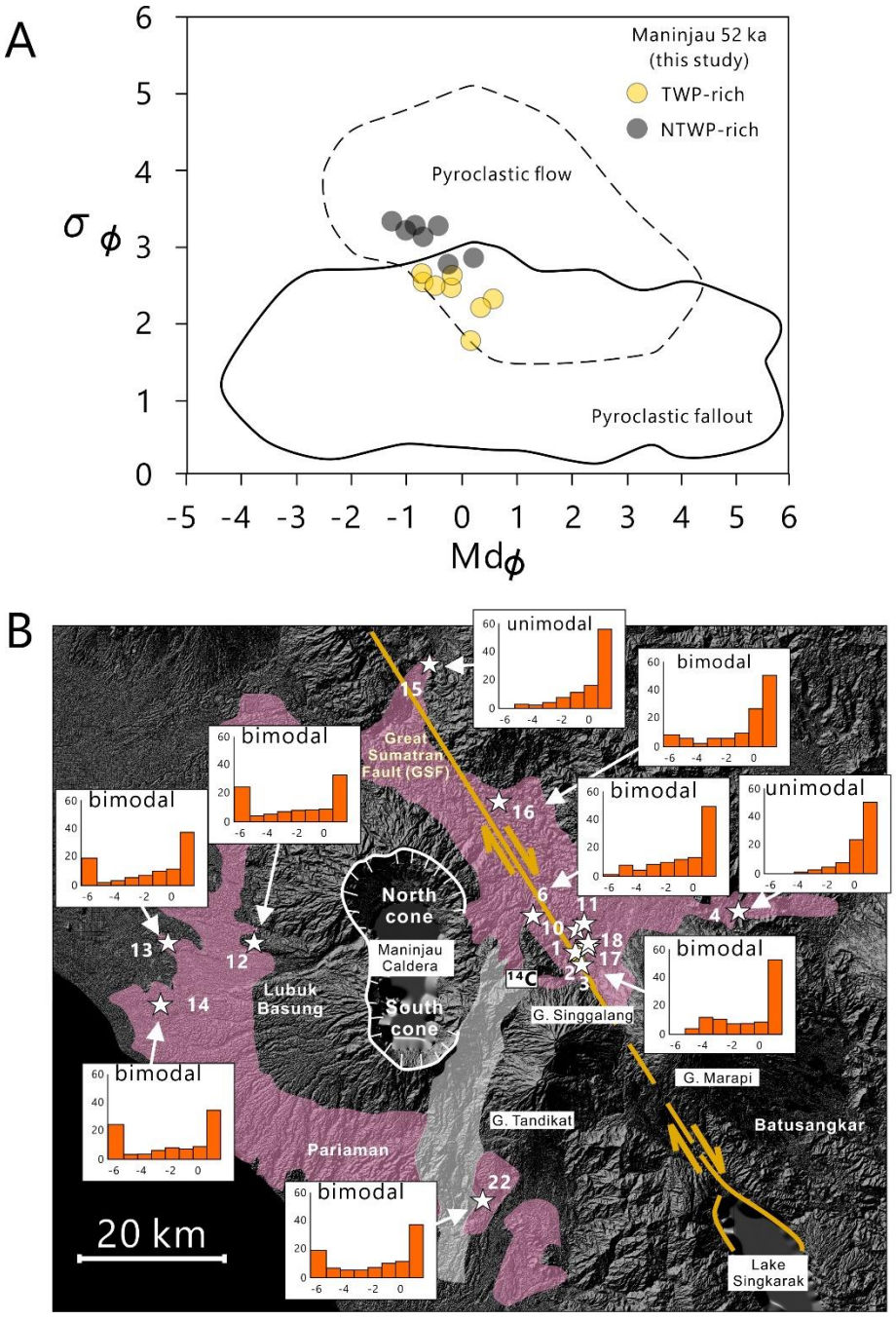

Figure 11. (A) Mdφ vs σφ plot and (B) variation of grain size distribution of the Maninjau 52 ka ignimbrite deposits.

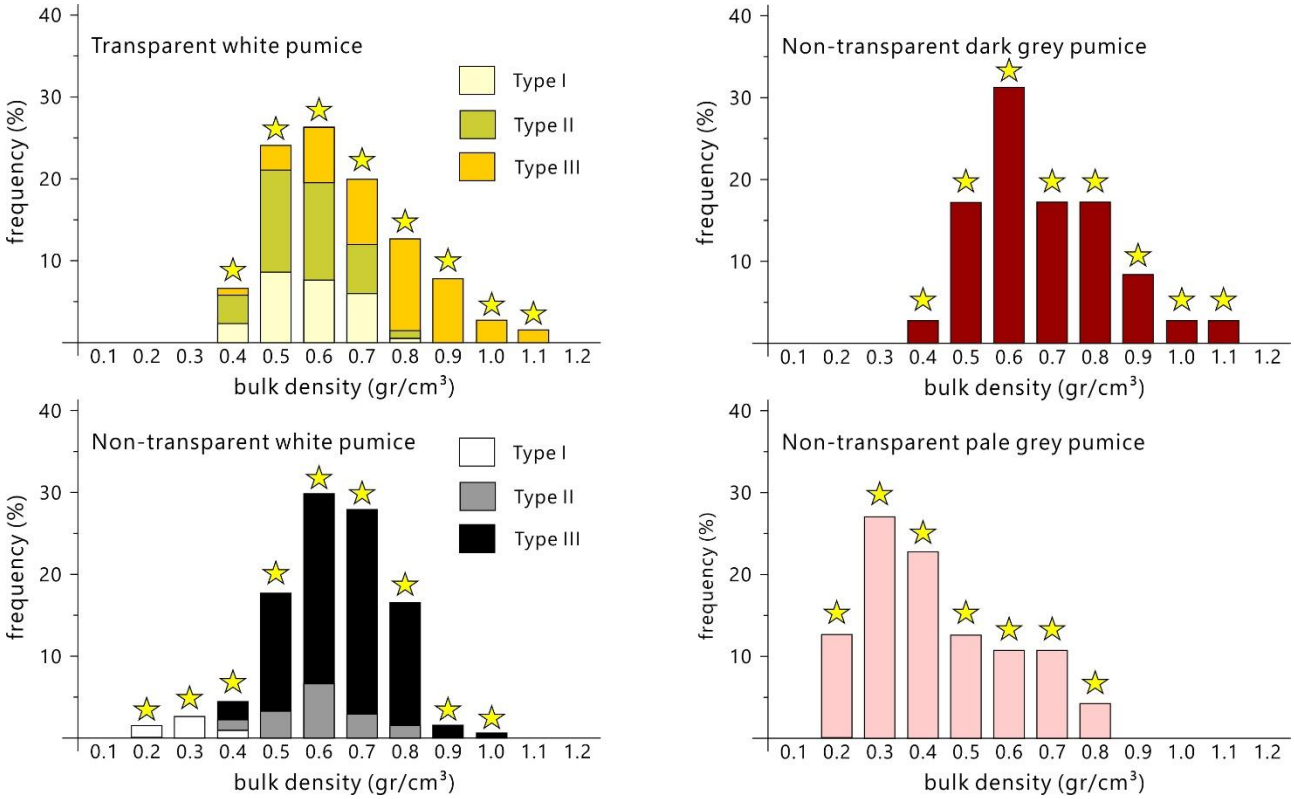

Figure 12. Bulk density variation of transparent white pumice (upper left), non-transparent white pumice (lower left), dark grey pumice (upper right), and pale grey pumice (lower right). Note the increasing pattern of bulk density from type I (spherical vesicle) to type III (elongated vesicle) in white pumice types.

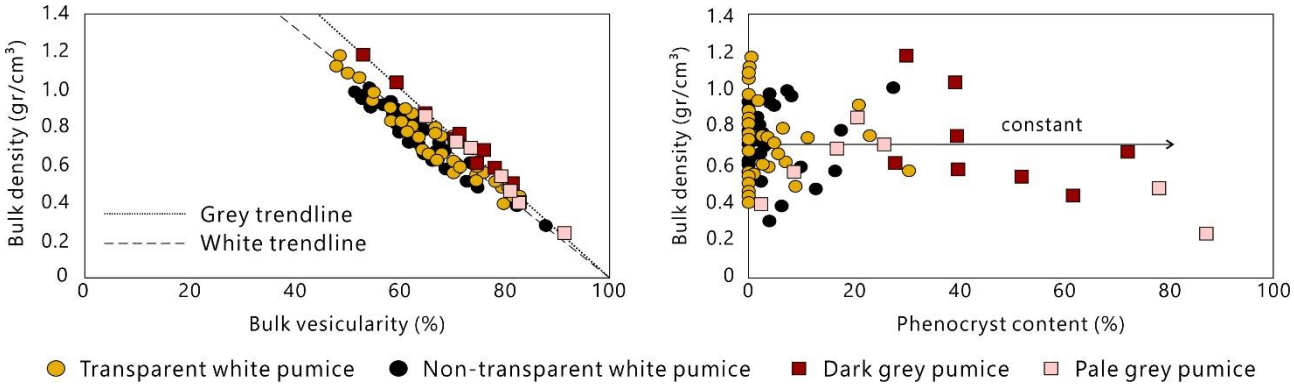

Figure 13. Correlation of bulk density, bulk vesicularity, and phenocryst content of all pumice types. Bulk vesicularity strongly controls bulk density, while phenocryst content has no effect for bulk density.

5.5. Petrography of the 52 ka juveniles

White pumice display a clearly distinctive petrographic features compared to grey pumice (**Fig. 14**). White pumice type is typically crystal poor, quartz-bearing, poor in mafic minerals (pyroxene and biotite), and amphibole-free. On the

other hand, grey pumice is characterized by an abundant crystal content, quartz-free, rich in mafic minerals, and amphibole-bearing. In addition, grey pumice's phenocrysts are highly fractured (and broken), while white pumice's phenocrysts are typically fine (**Fig. 14**).

5.5.1. White pumice

Transparent and non-transparent pumices are typically crystal poor, having 3.2 and 3.4 % of average crystal content (vesicle-free) for TWP and NTWP, respectively. Phenocryst phase from both white pumice types are plagioclase, quartz, and small amounts of biotite, pyroxene, and Fe-Ti oxides (**Fig. 14**). Transparent type has slightly larger average phenocryst size (0.31 mm^2) compared with non-transparent type (0.28 mm^2). Quartz phenocryst size vary from 0.05 to 7.5 mm^2, while plagioclase is smaller (0.07 to 3.9 mm^2), and other phenocrysts such as pyroxene, biotite, and oxide minerals are typically small (less than 0.05 mm^2). Although most of crystals grow as an individual crystal, some crystals form aggregates. Zoning textures (normal and oscillatory) are rarely found and only occur in plagioclase phenocrysts.

5.5.2. Grey pumice

Dark grey pumice (represent by GP 1 and BP 1) has 49 % of average crystal content (vesicle-free), as it consists of plagioclase (27 %), pyroxene (15 %), amphibole (3 %), biotite (1.7 %), Fe-Ti oxide (1 %), and minor amount of apatite (0.1 %) (**Fig. 14**). Most of the phenocrysts are relatively small (from 0.03 to 1.3 mm^2). Normal zoning texture is rarely observed and only occur in plagioclase phenocrysts, while oscillatory seems absent here.

Pale grey pumice (represent by GP 2 and BP 2) has a relatively lowest crystal content among grey pumices (avg. of 37 %, vesicle-free) with plagioclase as the main phenocryst phase (30 %) and the rest are pyroxene (4%), amphibole (2%), biotite (1%), and Fe-TI oxide (0.1 %) %) (**Fig. 14**). In terms of size, the phenocrysts vary from 0.05 to 6.2 mm^2. Normal zoning texture is rarely observed and only occur in plagioclase phenocrysts and there is no occurrence of oscillatory zoning.

Light grey pumice (represent by BP 3) has the most abundant crystal content (avg. of 60 %, vesicle-free), whereas plagioclase is dominating the phenocryst phase (51.6 %), followed by pyroxene (5 %), biotite (2.3 %), amphibole (1 %), and Fe-Ti oxide (0.1 %). Phenocryst sizes vary from 0.0 5 to 2.5 mm^2. Normal zoning textures are commonly observed in plagioclase phenocrysts. Rare oscillatory zoning also observed in some plagioclase phenocrysts. Honeycomb texture in plagioclase phenocryst becomes the hallmark that differs light grey pumice with the other pumice types (**Fig. 14**).

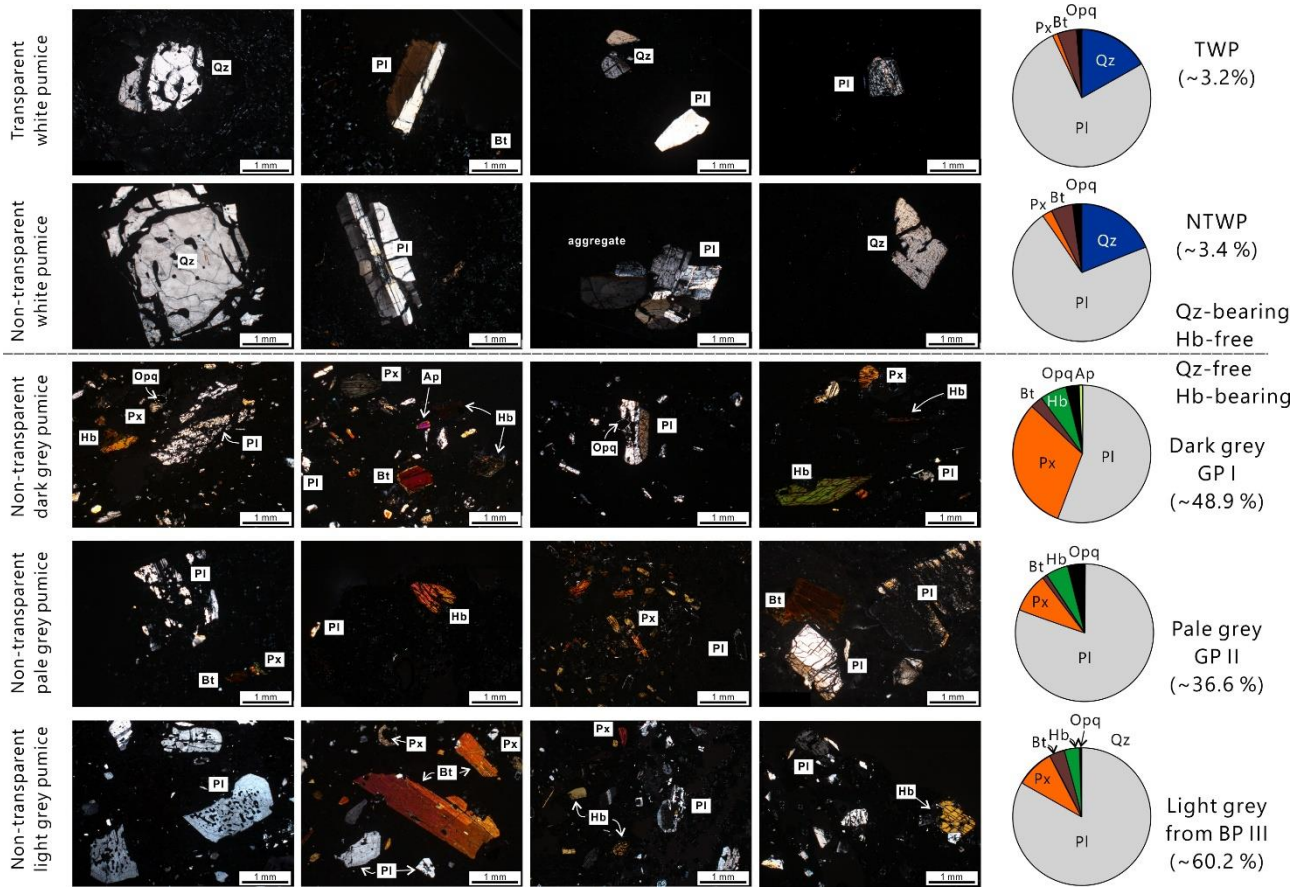

Figure 14. Petrographic images and modal mineralogy of white and grey pumice types. The modal mineralogy is shown by pie charts. Blue = quartz, grey = plagioclase, light brown = pyroxene, dark brown = biotite, dark green = hornblende, black = opaque minerals, and light green = apatite.

5.6. Glass and plagioclase compositions of the 52 ka juveniles

Glass compositions of TWP and NTWP are indistinctive and regarded as high-silica rhyolitic melts (avg. 78.5 wt. % SiO_2). Although there are no remarkable difference in terms of SiO_2, CaO, MgO, and anorthite contents, a slight difference in K_2O and Na_2O are observed between TWP and NTWP (**Fig. 15**).

Dark grey pumice has the relatively least evolved magma compositions, having only 74 % of average silica content with the highest MgO, CaO, Fe_2O_3, TiO_2, anorthite core compositions (avg. An_{67}), and lowest K_2O compared to all pumice types. Although pale grey and light grey pumices exhibit overlapping compositions in terms of silica (avg. 75.5 % for pale grey pumice and 76 % for light grey pumice) and the other major elements, and anorthite core compositions (avg.

An_{55} for GP 2 and An_{53} for GP 3), they are clearly distinctive in potassium. Particularly, light grey pumice has a higher potassium content compared to pale grey pumice (**Fig. 16**).

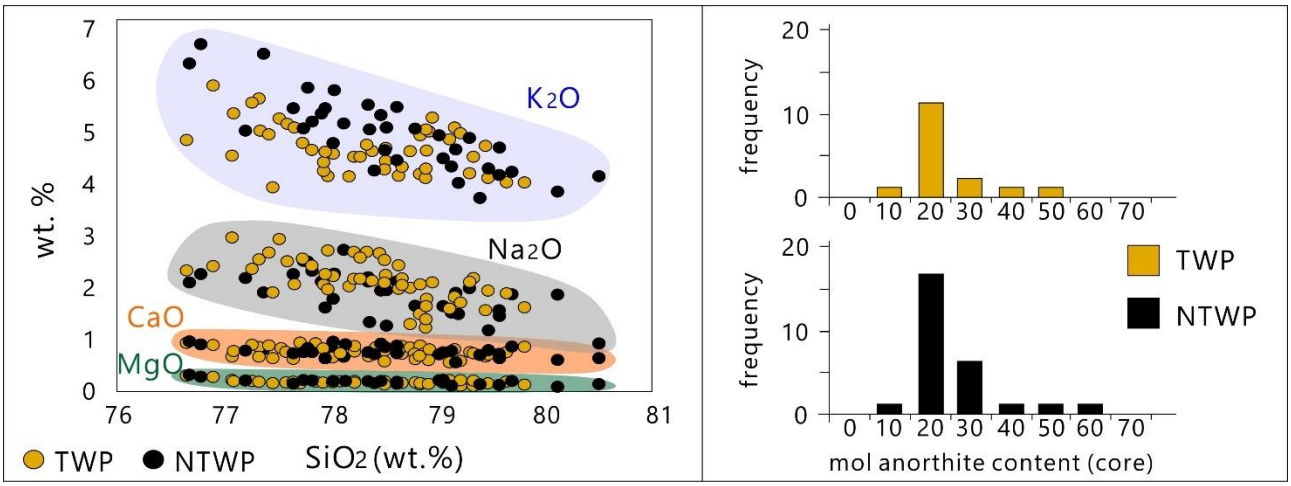

Figure 15. Comparison between transparent (TWP) and non-transparent (NTWP) white pumices in terms of glass (left) and plagioclase (right) compositions.

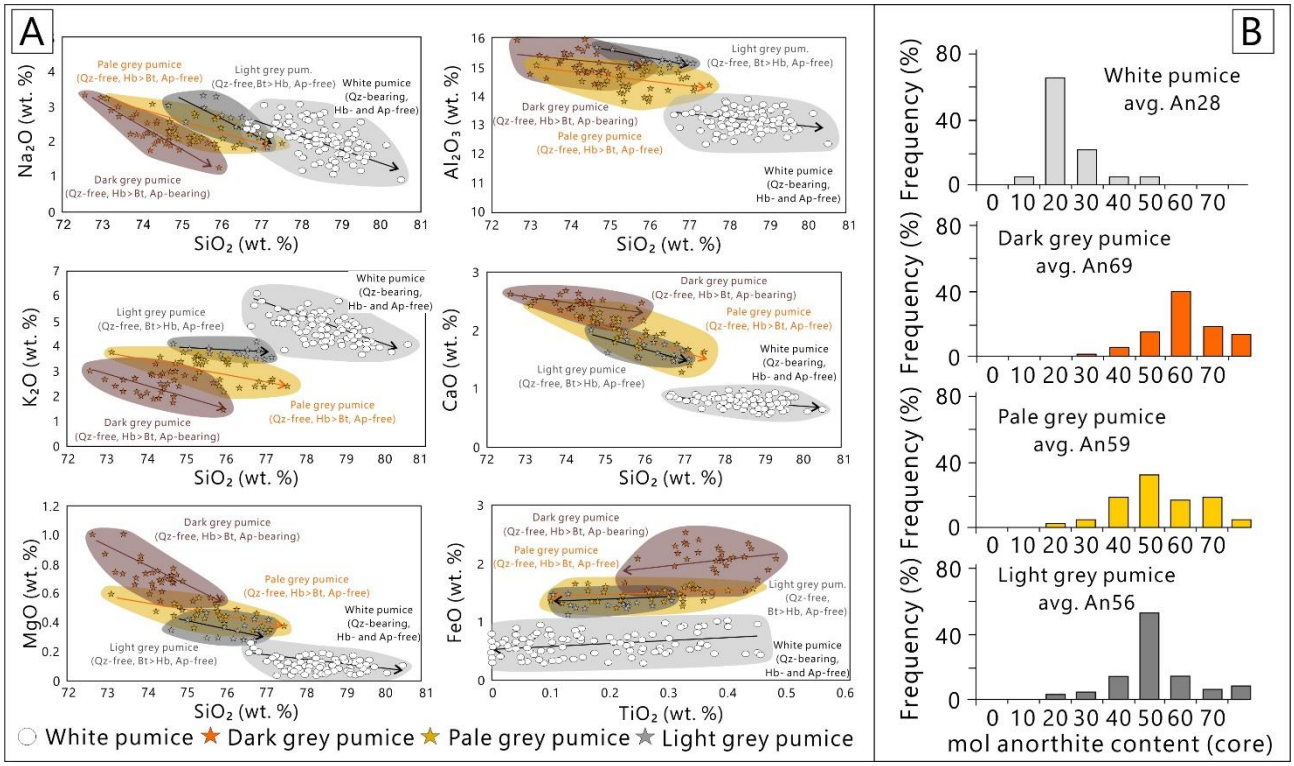

Figure 16. Comparison between all pumice types in terms of glass (left) and plagioclase (right) compositions.

5.7. Amphibole thermobarometry

All of the observed amphibole phenocrysts display unzoned texture (i.e., no compositional variations between the core and the rim) (**Fig. 17**). Therefore, in this study, we only report the core amphibole compositions in order to estimate the apparent temperature, pressure, and water content. Based on the amphibole core compositions data, it is found that all grey pumice types have relatively similar apparent temperature and water content **(Fig. 16)**, particularly 842-902°C and 4.7-5.9 wt.%, 843-916°C and 4.9-6.2 wt.%, and 859-921°C and 5.1-6.6 wt.% for dark grey, pale grey, and light grey pumices, respectively. While the apparent pressure are typically distinctive, as dark grey pumice is considered to be sourced from the shallowest grey magma (155-223 MPa), followed by the light grey (174-252 MPa) and pale grey (161-270 MPa) pumice.

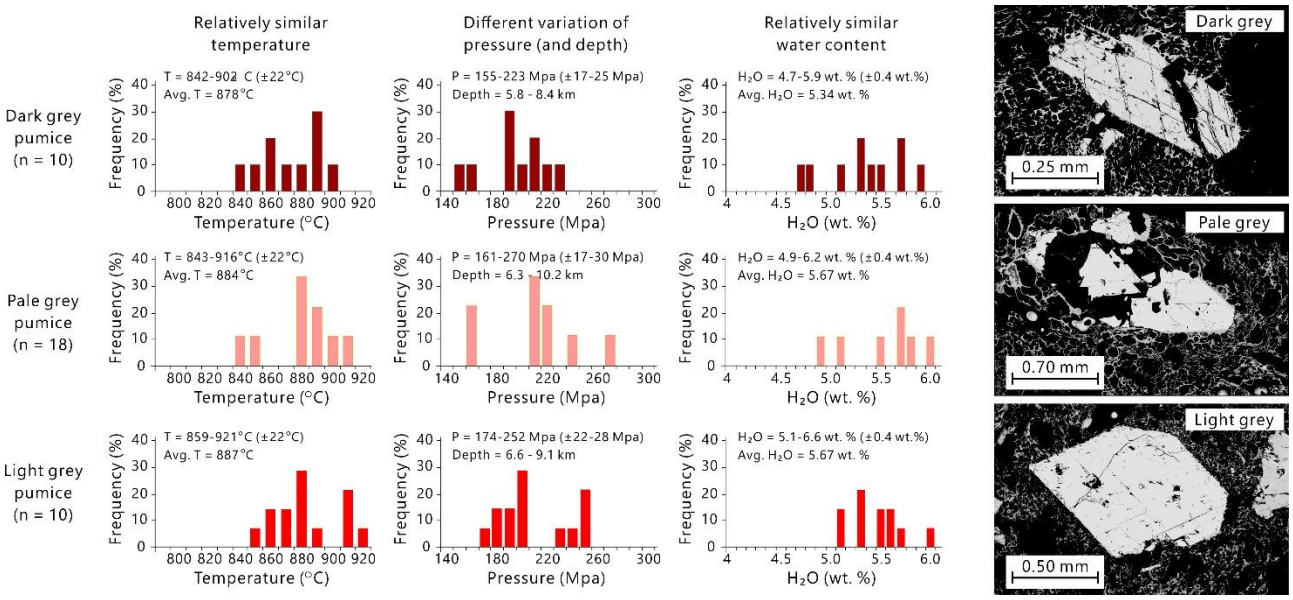

Figure 17. Histograms showing the result of estimated temperature, pressure, and water content for grey pumice types. Since there is no chemical variations in the amphibole phenocryst, we only report the core compositions.

5.8. Definition of pheno- and matrix-vesicles

Qualitatively we can clearly recognize the large-sized vesicles in pyroclast are considered as pheno-vesicle, and the small-sized vesicles in groundmass with relatively narrow size variation are considered as matrix-vesicle. To be quantitative, we used VSDs data (**Fig. 18**), which show that TWP contains smaller number of matrix-vesicle and larger number of pheno-vesicle compared with NTWP. Dark grey and light grey pumices seems to have small amount of pheno-vesicle and typically dominated by matrix-vesicle, while pale grey pumice contains moderate fraction of pheno- and matrix-vesicles. All pumice types show bimodal distribution of VSDs, where the decay of small and large-sized vesicle

populations are terminated at the beginning of second peak around 0.1 mm vesicle diameter. Therefore, we define the boundary between pheno-vesicle and matrix-vesicle by the vesicle diameter 0.1 mm.

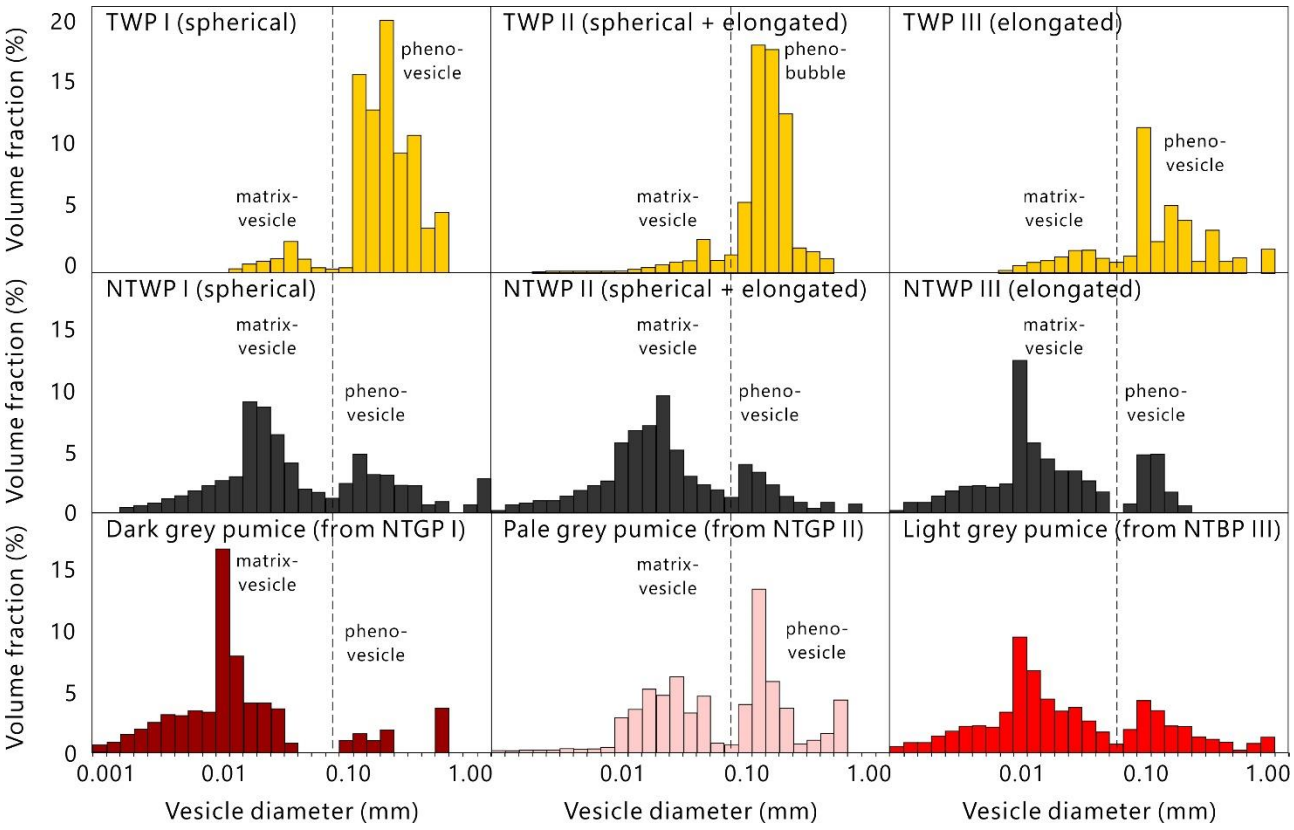

Figure 18. Vesicle size distributions (VSDs) of white pumices (TWP and NTWP, including the type I, II, and III) and grey pumices. All samples display bimodal distribution of VSDs. The boundary between pheno- and matrix-vesicles seems to be consistent, about 0.1 mm vesicle diameter.

5.9. Quantitative data of pheno- and matrix-vesicles

We found the negative correlation between pheno- and matrix-vesicle fractions (**Fig. 19**). Both transparent and non-transparent (including white and grey pumices) type also can be clearly distinguished based on the most dominant fraction between pheno- and matrix-vesicles. Transparent type is dominant in pheno-vesicle, whereas non-transparent type is dominant in matrix-vesicle (**Fig. 20**). Our data show that the NTWP and all of grey pumice types are located within the region of non-transparent type, conversely with TWPs which are located in the region of transparent type. In terms of white pumice, we found that the average size of pheno-vesicle and matrix-vesicle in transparent type are typically larger than non-transparent type. Note that volume fraction is positively correlated with average diameter, for both pheno- and matrix-vesicles (**Fig. 20A, B**). TWP has typically higher PVND than NTWP (**Fig. 20C**). TWP clearly show wider

variation and smaller MVND value compared to NTWP, hence also yield in lower matrix-vesicle volume fraction **(Fig. 20D**). Because matrix-vesicle is negatively correlated with pheno-vesicle, MVND will also result in negative correlation with size and volume fraction of pheno-vesicle (**Fig. 20E, F**). We found two types of correlation between PVND and MVND: (1) nearly constant correlation for TWP, and (2) negative correlation for NTWP (**Fig. 21**). Note the two different correlation pattern which are uniquely correlated to the pumice type. The nearly constant correlation correspond to the TWP, while the negative correlation correspond to the NTWP. For the comparison, we also show the correlation between PVND and MVND of grey pumice types (**Fig. 22**). Worthy to note, the correlation between PVND and MVND of grey pumices only result in negative correlation.

5.10. Magma decompression rate

We calculate the magma decompression rate on white pumice following Toramaru (2006) as follows:

$$\left|dP/dt\right| = a \cdot D \cdot \sigma^2 \cdot P_W^{-1/3} \cdot T^{-1/2} \cdot \mathrm{N_{mv}}^{2/3} \quad (6)$$

where a is a constant (1×10^{15}), D is the diffusivity of water in a silicate magma (m^2/s), σ is the interfacial tension (N/m), P_W is the initial saturation pressure (Pa), T is the temperature (K), and $\mathrm{N_{mv}}$ is the MVND. The initial saturation pressure and water concentration of the Maninjau 52 ka magma are estimated to be approximately 150 MPa and 5 wt. %, respectively (see discussion 6.2. for the detailed explanation). However, there is a lack of data on water diffusivity, interfacial tension, pressure, and temperature. Therefore, to accurately estimate the magma decompression rate, we obtain the water diffusivity (D), interfacial tension (σ), magma temperature (T) based on equations from Zhang and Behrens (2000), Bagdassarov et al. (2000), and Toramaru (2006) as follows:

$$T = 1000/0.16 + 0.01Cs \quad (7)$$

$$m = -20.79 - 5020/T + P \times 10^{-6}/1273 \quad (8)$$

$$D_{ZB2000}(C_W, T, P) = \mathrm{X} \cdot \exp(m)\{1 + \exp\left[56 + m + \mathrm{X} \cdot (-34.1 + 44620/T + 57.3\left(P \times 10^{-6}\right)/1273 - \sqrt{X}(0.091 + 4.77 \times 10^{-6}/T^2)\right)\right] \quad (9)$$

$$\sigma = 0.2366 \times \exp\left(-0.35 \times 10^{-8} \times P_w - 11 \times 10^3 \left(1/T - 1/1273\right)/R\right) \quad (10)$$

The temperature, water diffusivity, and interfacial tension of Maninjau magma are estimated to be approximately 1058° K, 8.9×10^{-12} m^2/s, and 0.1 N/m, respectively (for P_W = 180 MPa, and H_2O = 5 wt. %). Grey pumices were neglected because of the broad variability in the silica compositions and initial saturation pressure (**Fig. 15**).

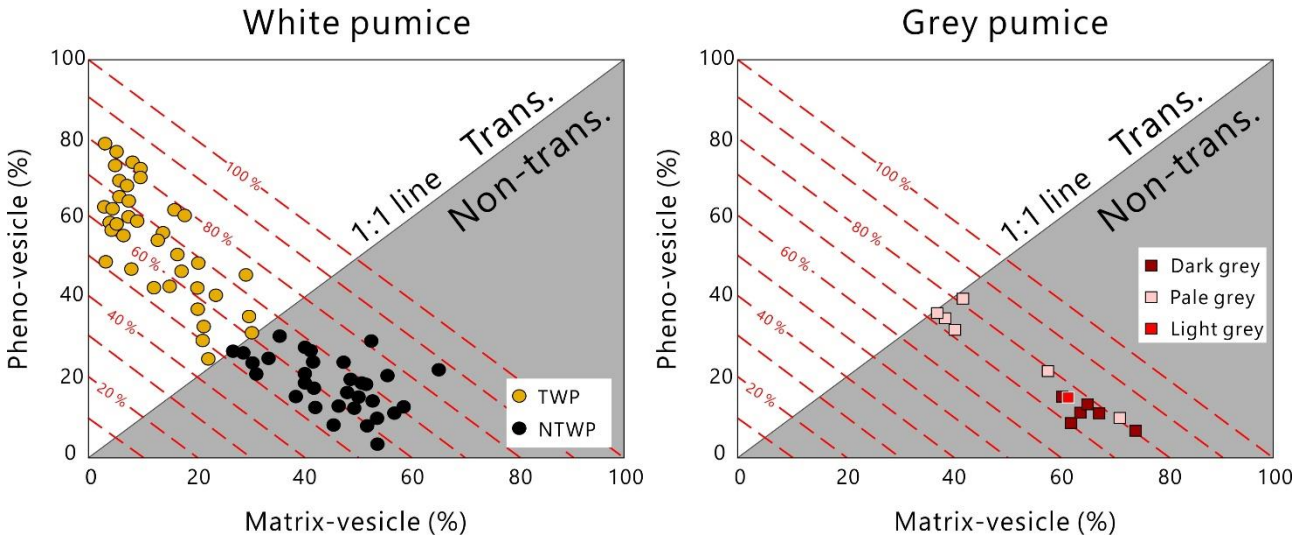

Figure 19. Volume fraction ratio between pheno- and matrix-vesicles of white and grey pumice types. Dashed red lines correspond to the linear relationship between pheno- and matrix-vesicles in any given bulk vesicularity.

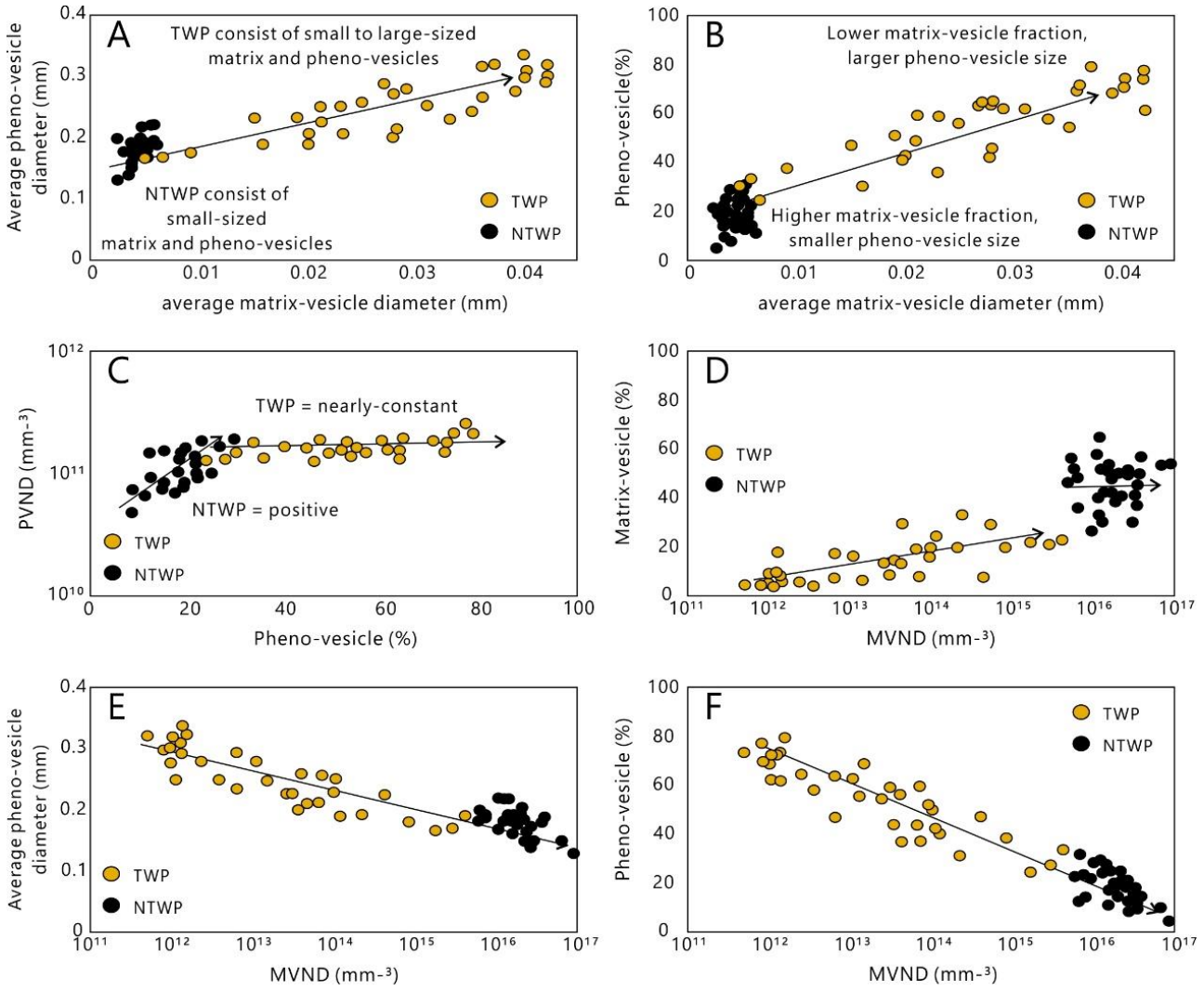

Figure 20. Textural parameter of the transparent and non-transparent white pumices. See text for discussion.

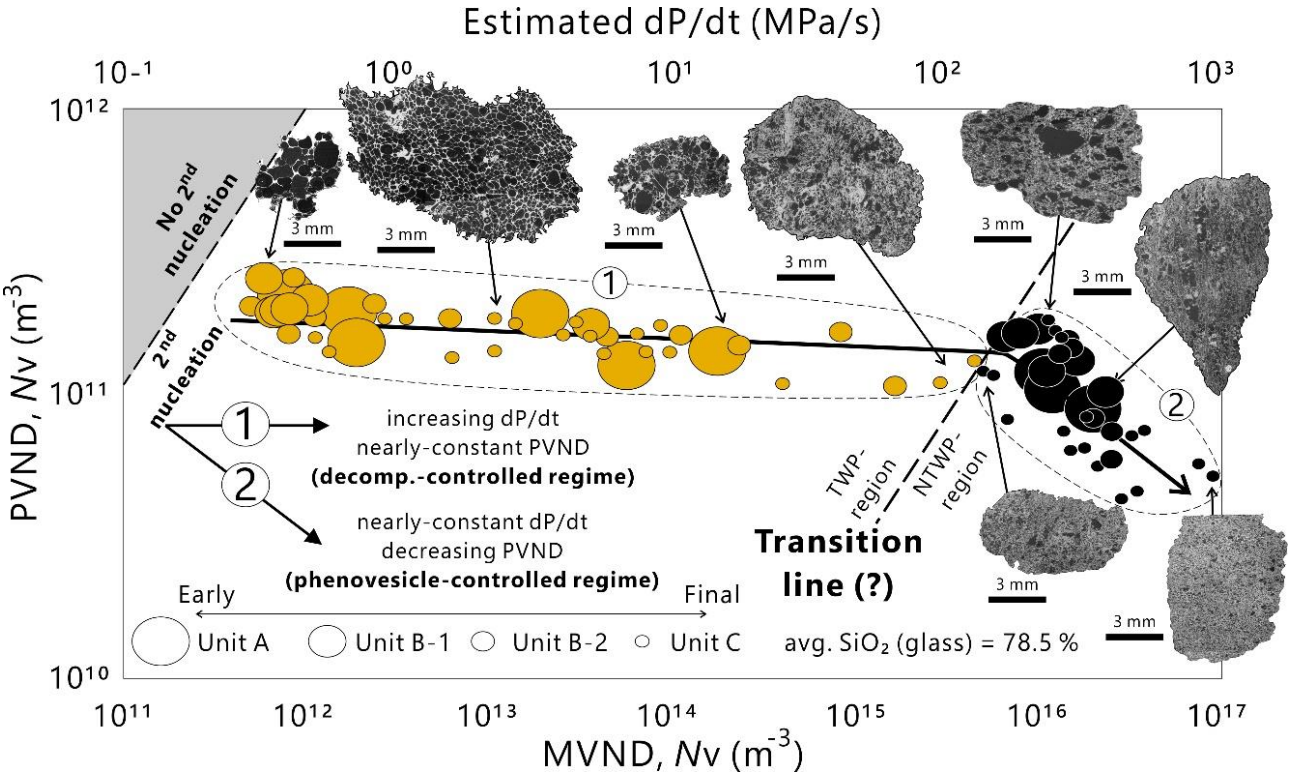

Figure 21. Pheno-vesicle number density (PVND) and matrix-vesicle number density (MVND) diagram of white pumice. Note the two different correlation pattern which are uniquely correlated to the pumice type. The first regime (decompression-controlled regime) correspond to the TWP, while the second regime (phenovesicle-controlled regime) correspond to the NTWP.

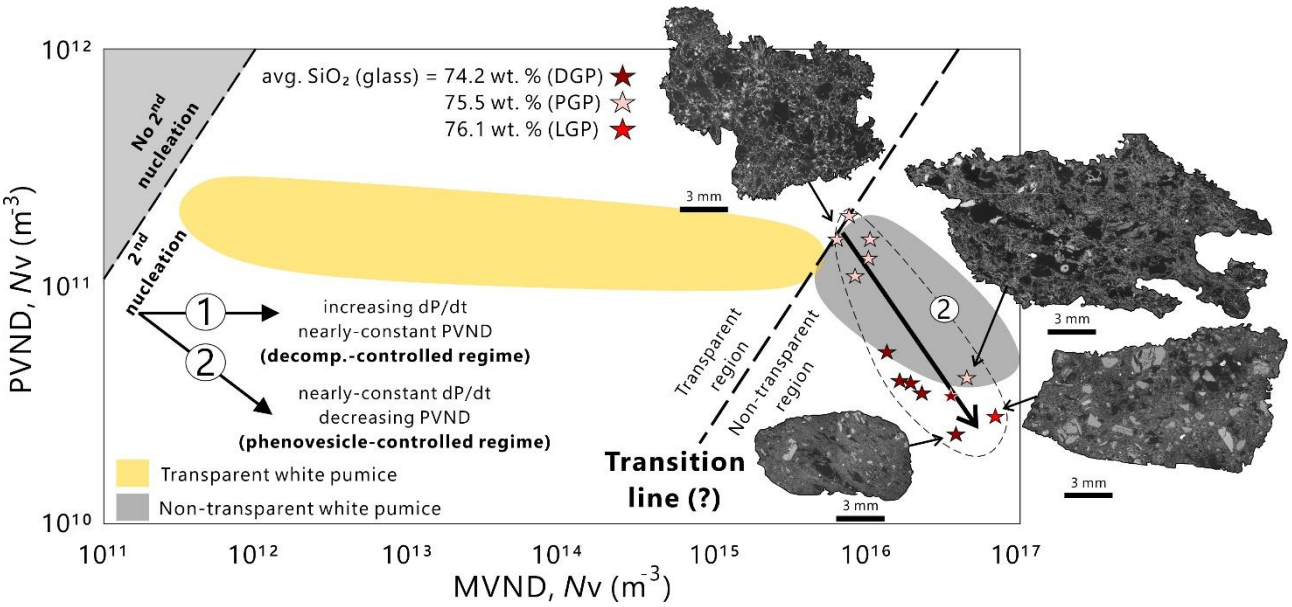

Figure 22. Pheno-vesicle number density (PVND) vs matrix-vesicle number density (MVND) diagram of grey pumices. All grey pumice types are located in the non-transparent region and only correspond to the second regime. Note that we do not show the decompression rate value because of the distinctive silica content between each grey pumice type.

6. Discussion

6.1. Magmatic origin

6.1.1. White pumice (TWP and NTWP)

Previous researchers have shown that Maninjau pumices (correspond to white pumice, either transparent or non-transparent type) have similar and homogeneous bulk and glass compositions (Leo et al. 1980, Alloway et al. 2004, de Maisonneuve and Bergal-Kulvikas 2020). However, they did not discriminate the pumice types for chemical analyses. Here, we confirmed that both TWP and NTWP at all deposit locations exhibit similar mineralogy characteristics and chemical compositions (**Fig. 15**). This suggest that both white pumice types were originated from the same giant, highly evolved, and nearly aphyric-rhyolitic magma chamber, which erupted at the same time. The slight variation in sodium and potassium between TWP and NTWP can be explained by the in-situ crystallization of Ab (Na)-rich plagioclase phenocrysts. In particular, higher crystallization of sodium-rich plagioclase in NTWP will reduce the portion of sodium and causes the relative increase of potassium in the melt.

6.1.2. Grey pumice (dark grey, pale grey, and light grey pumices)

In figure 1, we clearly show that white pumice and grey pumices are typically different in terms of mineralogy and chemical compositions. Namely white pumice were originated from a highly-evolved and crystal-poor magma, while grey pumices are characteristically sourced from a less-evolved and crystal-rich magma. Moreover, our data also suggest that each grey pumice type has different mineralogy and chemical compositions (**Fig. 16**). Dark grey pumice has the least evolved chemical compositions and the most abundant pyroxene and amphibole minerals among all of the grey pumice types. Moreover, the occurrence of apatite become the hallmark that differs the dark grey pumice with the other grey pumice types. As the magma become more differentiates to the more evolved compositions (toward the pale grey and light grey pumice, respectively), the amount of pyroxene and amphibole and the anorthite content decreases. Although the chemical compositions of pale grey and light grey pumice mostly overlaps, they are typically different in terms of potassium (light grey pumice has a slightly higher K_2O than pale grey pumice) and plagioclase texture (light grey pumice is characterized by an abundant honeycomb texture as it does not observe in other pumice types). This evidence strongly suggest that each grey pumice were originated from different magma chambers that experienced different processes, thus

referred as dark grey magma, pale grey magma, and light grey magma for the magmatic origin of each respective pumice types.

6.2. Magmatic reservoirs beneath the Maninjau caldera

Because quartz and amphibole are known to have different mineral stability (i.e., quartz is more stable in lower pressure while amphibole is more stable in higher pressure), their absence and/or occurrence can be used to qualitatively determine the relative position of the magma chamber. In this case, we suggest that white magma was stored in a relatively shallower position compared to all of the grey magmas due to the absence of amphibole and the abundance of quartz. Therefore, we roughly assume that the white magma chamber was stored at some pressure level less than 155 MPa (probably 150 MPa for white magma) with less than 5.3 wt. % of H_2O (probably 5 wt. % H_2O for white magma), which is correspond to the minimum pressure and water content of the shallowest grey magma (dark grey magma). The fact that grey pumices have more abundant hydrous minerals (biotite and amphibole) compared to white pumice does not deny this idea. Namely water is an essential component for crystallizing any hydrous minerals, therefore, the more abundant hydrous minerals correspond to the higher crystallization pressure due to the higher water content (McBirney 2007).

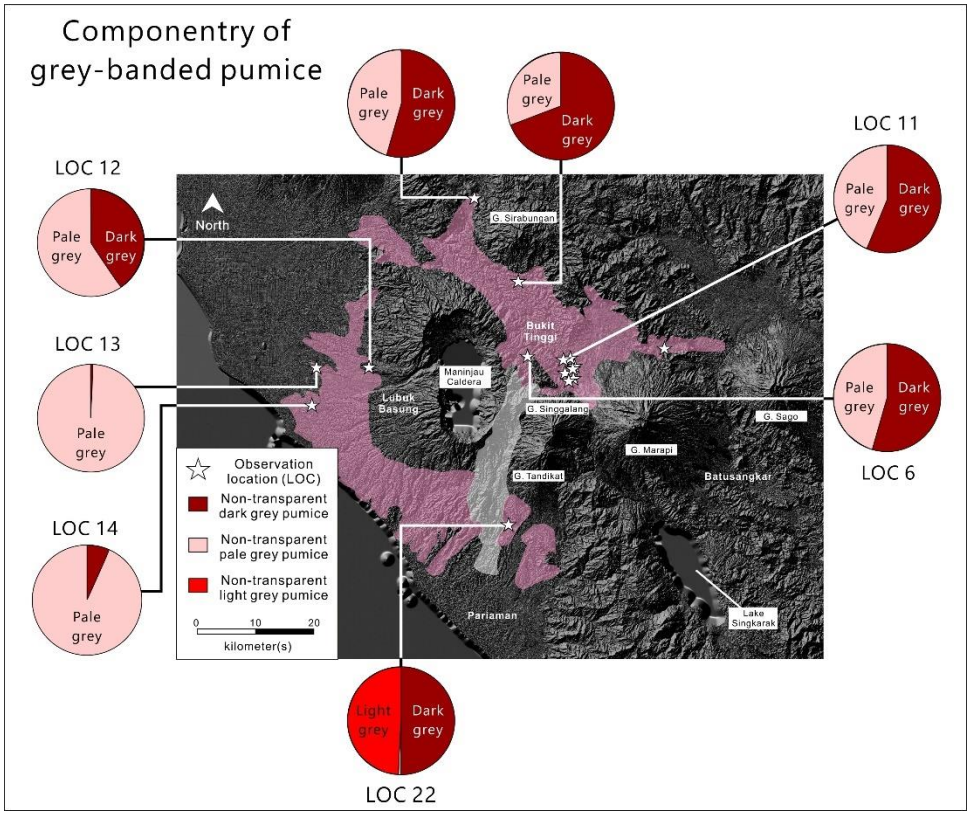

Figure 23. Component distribution of grey and banded pumices. Red, darker red, and pink corresponds to light grey pumice, dark grey pumice, and pale grey pumice, respectively.

Because we dealt with an ignimbrite deposits, such component distribution strongly depends on the direction of the eruption (not controlled by the wind's direction, i.e., Plinian eruption) and therefore, creating a unique spatial distribution relative to the source. Hence, we attempted to estimate the position of the grey magmas via the component distribution of the grey (and banded) pumices **(Fig. 23)**. Based on the component distribution, we found that light grey pumice only exist in the southern deposit, while dark grey pumice and pale grey pumice are distributed to all directions. However, the occurrence of dark grey pumice is considerably minor in the western deposits and pale grey pumice is almost absent in the southern deposit. Based on this evidence, we suggest that dark grey, pale grey, and light grey magmas were positioned in eastern, western, and southern positions **(Fig. 24)** relative to the central part of the Maninjau caldera.

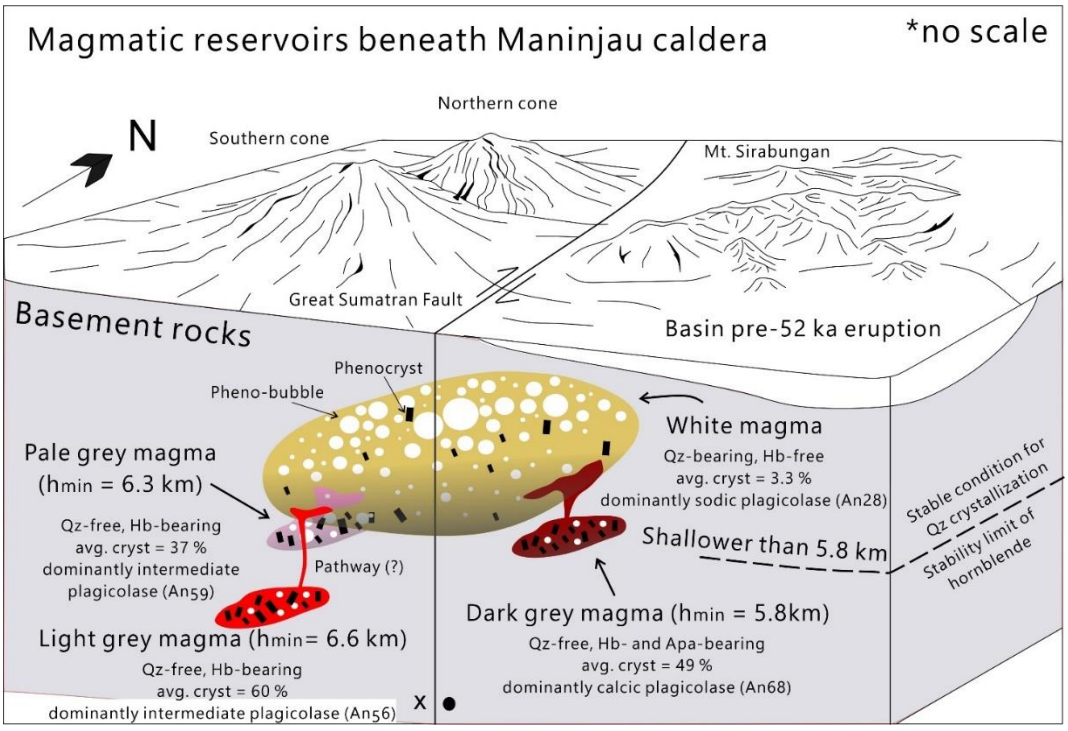

Figure 24. Sketch of the syn-eruptive magmatic reservoirs beneath the Maninjau caldera. Note the anorthite content correspond to the average value. See text for discussion.

6.3. Formation of transparent and non-transparent pumice: role of volume fraction

In figure 19, we can confirm quantitatively the negative correlation between pheno- and matrix-vesicles. This indicate that pheno- and matrix-vesicles are competing to reach supersaturation level (i.e., the existence of pheno-vesicle can limit the supersaturation of matrix-vesicle) (Toramaru 2014). Furthermore, such competition will determine the resultant pumice type as it clearly defined by the volume fraction ratio of pheno- and matrix-vesicles (**Fig. 19**). Namely if the rising magma is dominated by pheno-vesicle (above the equal line), second nucleation will be limited and thus results transparent type. Conversely, if the rising magma lacks pheno-vesicle, second nucleation significantly takes place

and thus results non-transparent type. Therefore, despite the chemical differences between white and grey pumices, it can be simply inferred that; transparent pumice originates from phenovesicle-dominated magma, while non-transparent pumice dose from pheneovesicle-poor magma.

6.4. Correlation of PVND and MVND: role of magma decompression rate and pheno-vesicle abundance

There are two important factors which are essentials for controlling the relationship between PVND and MVND. The first factor is the magma decompression rate (dP/dt). Toramaru (2006) stated that MVND is proportional to 3/2 power of decompression rate. Therefore, we can expect that higher MVND value is generated by higher magma decompression rate, which might occur during the development of caldera. The best natural example of this condition are the 182 ka eruption of Santorini-Lower Pumice 1, the 7.7 BP eruption of Mazama, and the 1991 AD eruption of Pinatubo (Simmons et al. 2017; Klug et al. 2002; Polacci et al. 2001), where the MVNDs value increase from the early stage to the final stage. The second factor is be related to the distribution of pheno-vesicles in pre-eruptive magma chamber. It is known that the overgrowth of pheno-vesicles will increase the total surface area and depletion of gas in melt, hence diminishing the supersaturation (Toramaru 2014). Consequently, if the decompression rate is constant, second nucleation will be limited when the uprising magma contains such high number density of pheno-vesicles. Otherwise, second nucleation can effectively take place under the high PVND condition if the decompression rate is high enough (Toramaru 2014). The critical condition whether the second nucleation occurs or not under the certain decompression rate is simply represented by the similar values of PVND to MVND expected to take place by the decompression rate. In our case, the 10^{11} m^{-3} is an approximate critical value: the second nucleation start to take place when the decompression rate exceeds the enough value, about 0.1 MPa/s (**Fig. 21**).

In this study, we found that both conditions are observed in the most dominant product of the Maninjau 52 ka eruption (white pumice). TWP is characterized by the high PVNDs value, suggesting that TWP magmas were extremely rich in pheno-vesicle (**Fig. 21**). Interestingly, under the constantly high-PVND condition, TWP magmas were able to produce four different magnitudes of MVNDs value and its variation can be expressed by the function of time (**Fig. 21**). Particularly, as the eruption undergoes to the final stage, the MVND gradually increases. This suggests that, starting with a mild decompression, magma decompression rate increases towards the formation of caldera. On the other hand, NTWP show such monotonic steep decrease in PVNDs value together with the slight increase in MVNDs value. This condition likely corresponds to our second factor, that is, the decrease in pheno-vesicle content (in nearly constant decompression rate) with time, leading to increase in supersaturation for matrix-vesicle nucleation (**Fig. 21**). The transition from TWP-

rich to NTWP-rich deposits coupled with the fact of decreasing pheno-vesicle content from the lower until upper stratigraphic level becomes an important evidence for the indication of pheno-vesicle stratification in magma chamber (**Figs. 10 and 24**). We suggest that the phenovesicle-rich magmas were evacuated during the early stage under the initially mild and subsequent high decompression rate, producing TWP-rich ignimbrites (unit A and B), and thus followed by the emplacement of phenovesicle-poor magmas from the lower part that produces NTWP-rich ignimbrites (unit C).

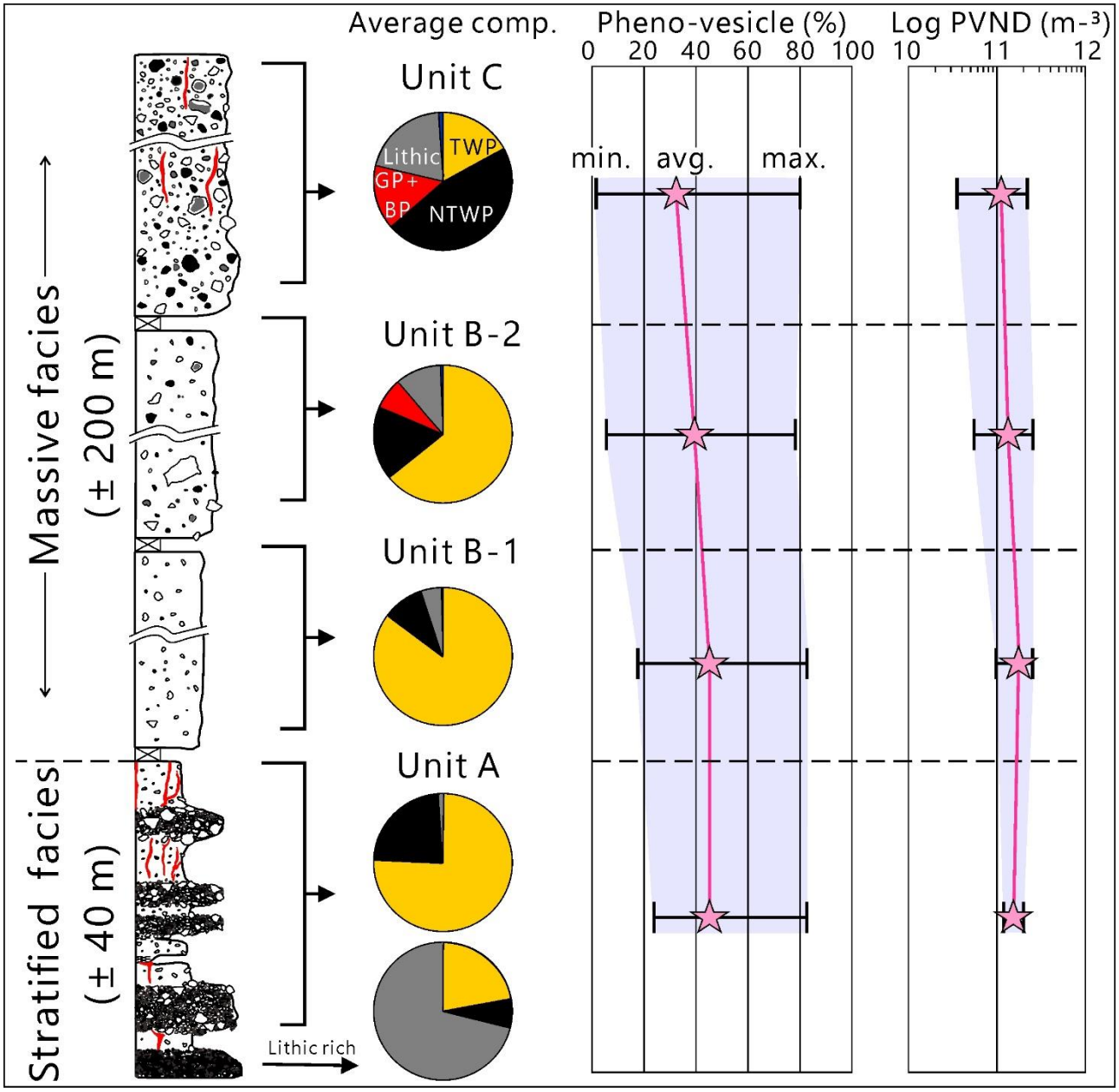

Figure 25. Correlation between componentry, pheno-vesicle abundance, and pheno-vesicle number density (PVND) from the lowermost to the uppermost stratigraphic section. Note that stratigraphic position is inversely proportional with the position in the magma chamber, suggesting a pheno-vesicle stratification in the pre-erupte white magma chamber.

In terms of grey pumice, it is found that all grey magmas experience high magma decompression rate thus responsible for nucleating such an intense amount of matrix-vesicle (represent by high MVND, larger than $10^{16}mm^{-3}$) and furthermore, allowing these grey magmas to reach the supersaturation level of matrix-vesicle thus results in non-transparent type (**Fig. 22**). The fact that these grey magmas are absent during the early stage (unit A and B-1) and dominantly exist in unit C become the reason why grey magmas experience only such high magma decompression rate. During this nearly constant condition of a high magma decompression rate, the supersaturation of matrix-vesicle increases as a result of decreasing PVND (in the uprising magma) which is correspond to the second regime (**Fig. 22**).

6.5. Why transparent type is uncommon?

To generate an explosive eruption, especially a large magnitude caldera-forming eruption (VEI>7), a supersaturation of pheno-vesicle must have been established first in order to provide magma chamber overpressure, at least theoretically (Huppert and Woods 2002). Therefore, by assuming a same level of supersaturation of pheno-vesicle (high PVND) to the other caldera-forming eruptions (at least same magnitude), a high magma decompression rate is essentially needed in order to attain the supersaturation of matrix-vesicle and thus generate the common pumice type (non-transparent). For example, the MVNDs value of the 6.6 ka Mazama eruption are typically vary from 0.6 to $1\times10^{16}mm^{-3}$ (Klug et al. 2002). By assuming a maximum $2.5\times10^{11}mm^{-3}$ PVND value, the plot of the Mazama pumices will be plotted in the NTWP-region. In this case, because the 52 ka Maninjau eruption is found to have a predominantly low magma decompression rate, most of the erupted magmas cannot attain such supersaturation of matrix-vesicle and thus results in an extremely abundant formation of transparent white pumice (**Fig. 21**). Moreover, there is possibility that a high magma decompression rate will be led to the extensive formation of glass shards due to its high fragmentation-intensity. The lack documentation of co-ignimbrite ash deposits from Maninjau and its abundant large pumice fragments (**Figs. 4 and 5**) does not deny this idea.

6.6. Reconstruction of the 52 ka eruption

The eruption started by the vent-opening stage as indicated by the occurrence of lithic-concentrated zone (LCL) in the lowermost portion of the deposits (**Figs. 10 and 26**). The occurrence of numerous stratifications of PDC units might suggest that the eruption plume was relatively unstable and represent the condition of low magma discharge rate (Druitt and Sparks 1984; Allen 2000; Reubi and Nichols 2002). During this stage, a series of PDC deposits that fed from the phenovesicle-rich magma zone (upper portion of the white magma chamber) were emplaced to the eastern side and formed

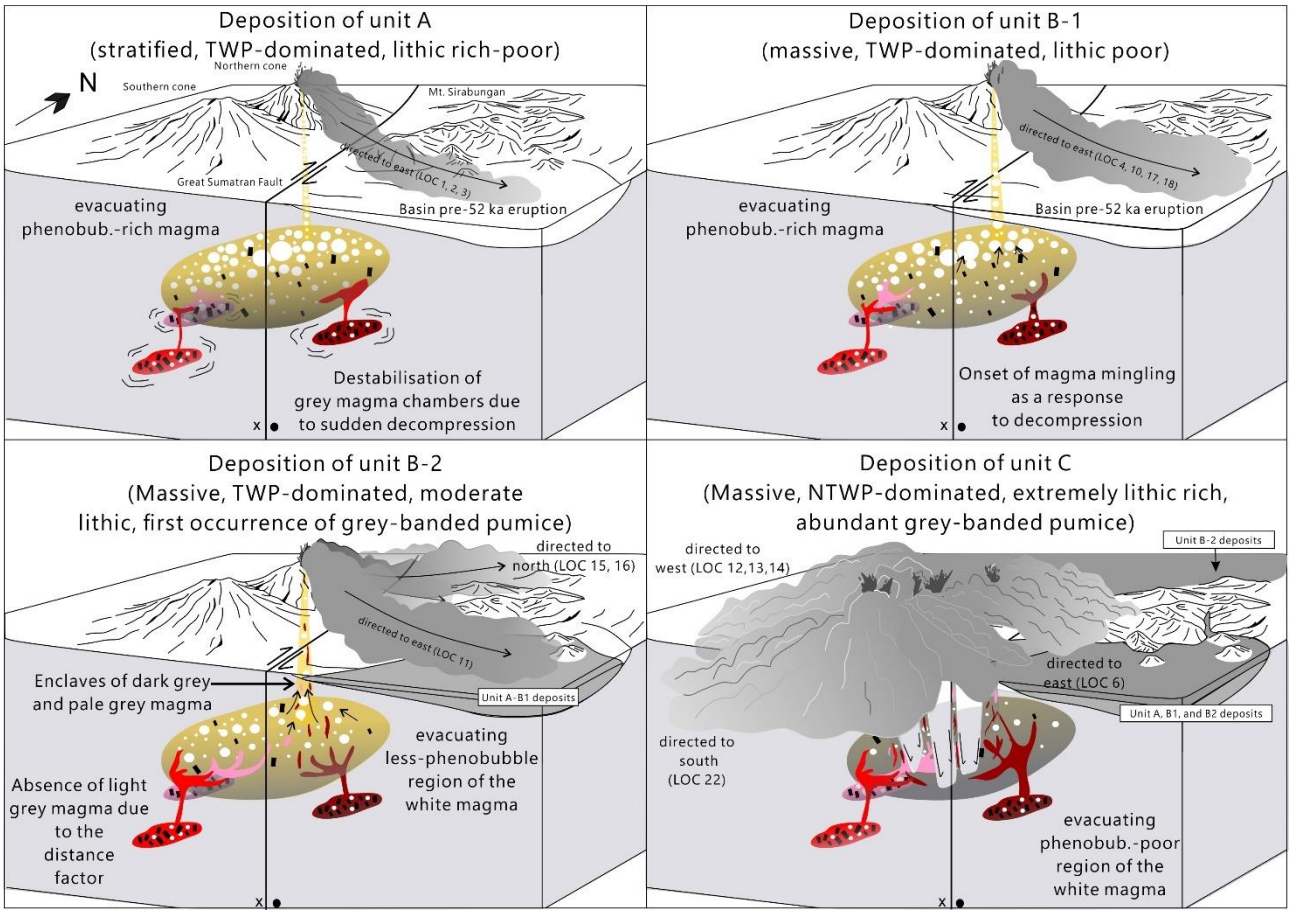

Figure 26. Cartoon showing the reconstruction of the 52 ka Maninjau eruption. See text for discussion.

a TWP-rich and stratified ignimbrite deposit (unit A) (**Fig. 26**). As the time goes, the eruption continues to evacuate magmas from the phenovesicle-rich magma zone, depositing the unit B that dominantly consists of TWP. An increase in magma discharge rate is expected to occur during the emplacement of unit B, as it indicated by the formation of massive ignimbrite just after the deposition of stratified deposits (**Figs. 10 and 26**) (Allen 2000; Reubi and Nichols 2002). We assume that the mingling between grey and white magma starts to take place during the deposition of unit B-1 as a response to destabilization led by sudden decompression (**Fig. 26**), and therefore erupted simultaneously during the deposition of unit B-2. The reason why the distribution of unit A and B are restricted to the eastern and northern side is probably due to the presence of a major fault named 'The Great Sumatran Fault' (GSF) which located in the eastern side of the caldera (**Figs. 2 and 26**). Such major structure is likely responsible for providing a weak zone due to the dense population of structures, and ultimately, become the pathway for magma for generating an eruption (Bellier and Sebrier 1994, Fernández-Blanco et al. 2016, Acocella et al. 2018). Finally, the eruption reached its climatic phase as it evacuate magmas from the phenovesicle-poor zone (**Fig. 26**), depositing a massive and NTWP-rich ignimbrite (unit C). The

abundant proportion of lithics and the radial distribution of the ignimbrite strongly suggests the very high magma discharge rate condition and the formation of another new vents throughout the caldera ring-fault system during the onset of caldera collapse (Allen 2000; Reubi and Nichols 2002; Seggiaro et al. 2019). Finally, the increasing proportion of basement lithics and grey-banded pumice from unit A to C suggest the progressive magma withdrawal from the relatively shallower to deeper origin (**Fig. 26**). Such eruption chronology is also can be observed in the deposits of the 182 ka eruption of Lower Pumice 1-Santorini, the 39 ka eruption of Campi Flgrei, and the 7.7 BP eruption of Mazama (e.g., Simmons et al. 2016, Simmons et al. 2017; Rosi et al. 1996; Suzuki-Kamata et al. 1993).

6.7. The absence of Plinian fall deposits

Caldera-forming eruptions are usually initiated by Plinian eruption and terminated by the formation of extensive pyroclastic density currents (PDCs) such as the 1.26 Ma eruption of Valles, 182 ka eruption of Santorini eruption, the 7.7 ka eruption of Mazama (Crater lake), the 7.3 ka eruption of Kikai, the 1257 AD eruption of Samalas (Rinjani), the 1815 AD eruption of Tambora, and the 1883 AD eruption of Krakatau (Goff et al. 2014; Simmons et al. 2017; Klug et al. 2002; Maeno and Taniguchi 2007; Vidal et al. 2015; Sigurdsson and Carey 1989; Nadeau et al. 2021). However, we found that the 52 ka Maninjau caldera-forming eruption experience no Plinian eruption, as indicated by the direct contact between the 52 ka ignimbrite with the paleosoil at LOC 15 and 16 (**Fig. 5**), making this eruption become one from a few examples of Plinian-free caldera-forming eruption such as the Toba, Ranau, and Aso (Chesner and Rose 1991; Natawidjadja et al. 2017; and Kaneko et al. 2007).

It is known that an eruption mechanism (collapsing column or convective plume) is a function of conduit radius, magma ascent rate, water content, and magma discharge rate (Wilson et al. 1980) (**Fig. 27**). In the case of a relatively similar variation of ascent rate (as a function of decompression rate) and water content as the present case, the conduit radius control those. Namely the fact that Maninjau 52 ka eruption experience small and very high magma decompression rate (**Fig. 21**) without producing any Plinian fall suggest that the conduit radius must be very large, robably larger than 600 m (**Fig. 27**). Since the formation of an extremely large conduit radius is unlikely to occur during the 'vent-opening' process, an external factor such as major structure (i.e., fault) is highly necessary for the establishment of a large conduit system. Therefore, we suggest that the occurrence of the "Great Sumatran Fault" might be responsible for providing a large conduit, and subsequently, resulting in a Plinian-free caldera-forming eruption (**Figs. 2 and 27**). Moreover, the fact that Ranau and Toba calderas are also associated with the "Great Sumatran Fault" system does not deny this idea.

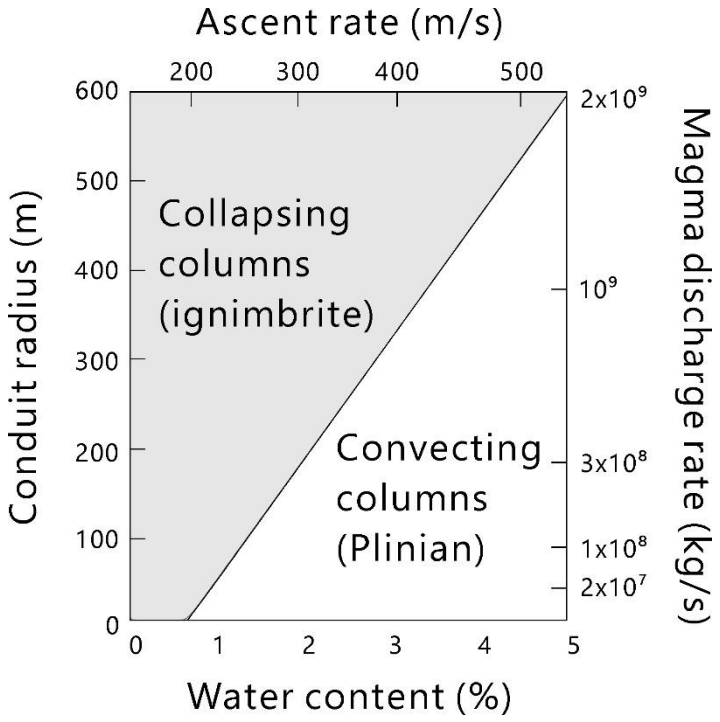

Figure 27. A figure showing the correlation between conduit radius with magma ascent rate, water content, and magma discharge rate with (redrawn from Wilson et al. 1980). The fact that Maninjau 52 eruption experience small and very high magma decompression rate without producing any Plinian fall suggest that the conduit radius was very large (probably more than 600 m).

6.8. The effect of pumice type in grain size distribution

In general, the abundance of ash particles can be used as a proxy to estimate the degree of fragmentation (Walker 1973). Namely a highly explosive eruptions are characterized by the high abundance of ash particles and *vice versa*. In this study, we found that Maninjau is an exceptional case. As we mentioned in previous section, we found that the decompression rate increase from the early (unit A-B) to the final (unit C) eruption stages. Therefore, the early and final eruption stages should preserve the smallest and largest portion of ash particles (or larger and smaller median GSDs value), respectively. However, our data suggest the opposite: the early eruption stage has the most abundant fraction of ash with smaller median values, while the final eruption stage represent the most substantial number of large particles with a higher median value. In order to explain this phenomenon, it is important to mention that (1) white pumice (either TWP and NTWP, which represent as the main juvenile product) is dominated by elongated-vesicle type, (2) the early eruption stage has more abundant portion of spherical vesicle (type I) than the final eruption stage, (3) transparent white pumice is typically fragile, while non-transparent white pumice is characteristically strong, and (4) the early and final eruption stages are dominated in transparent and non-transparent white pumice (**Fig. 10**). Therefore, the dynamics during syn-eruptive and syn-depositional processes such as fragmentation and erosional effect might be important.

A study from Heiken and Wohletz (1991) and Mertel et al. (2000) have revealed that vesicle shape in an ascending magma controls the fragmentation behavior. In particular, magmas with predominantly elongated vesicles are more resistant toward fragmentation because the vesicle connectivity is low compared to the magmas that contains spherical vesicle. As a result, the fragmented grains of magmas with elongated vesicle (final eruption stage) will be typically larger than any magmas that are containing more spherical vesicles (early eruption stage) and *vice versa* (**Fig. 28**). Such interpretation is appropriate with our dataset, as we show in figure 29 that the coarser ignimbrite (i.e., higher fraction in large grains) are typically dominated in type III pumice (elongated vesicle, either TWP or NTWP), while the finer ignimbrite shows higher fraction of type I and II pumices (**Fig. 29**). Therefore, we suggest that the first and second factor are likely controlled by the primary fragmentation processes.

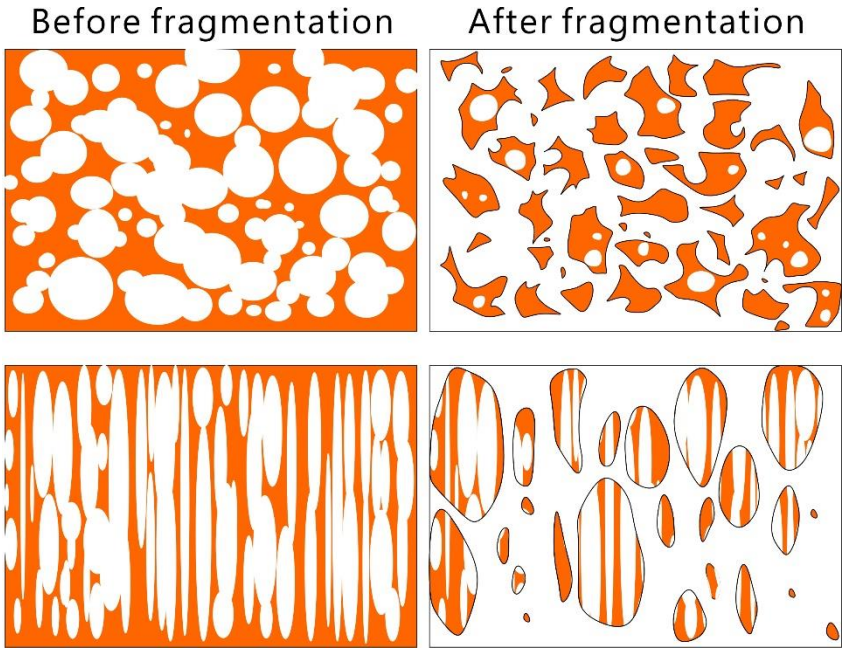

Figure 28. Different vesicle types result in different response toward fragmentation process (redrawn from Heiken and Wohletz 1991)

The third and fourth factors are likely corresponding to the syn-depositional process, as modification in the GSD due to the erosional processes (during the transportation of the PDC) cannot be neglected if the ignimbrite contains a highly abundant fragile juvenile type, that is, transparent white pumice. By contrasts, any NTWP-rich ignimbrite deposits might preserve a relatively more reliable and original GSDs as the juveniles are typically more resistant toward the erosion (i.e., western ignimbrite) (**Fig. 30**). This idea is supported by the fact that TWP-rich ignimbrite (i.e., eastern ignimbrite) is characterized by more abundant portion of dense and glassy ash particles than the NTWP-rich ignimbrite (i.e., western ignimbrite), which is likely to be originated from the eroded TWP as it is lacking matrix-vesicle (**Fig. 30**)

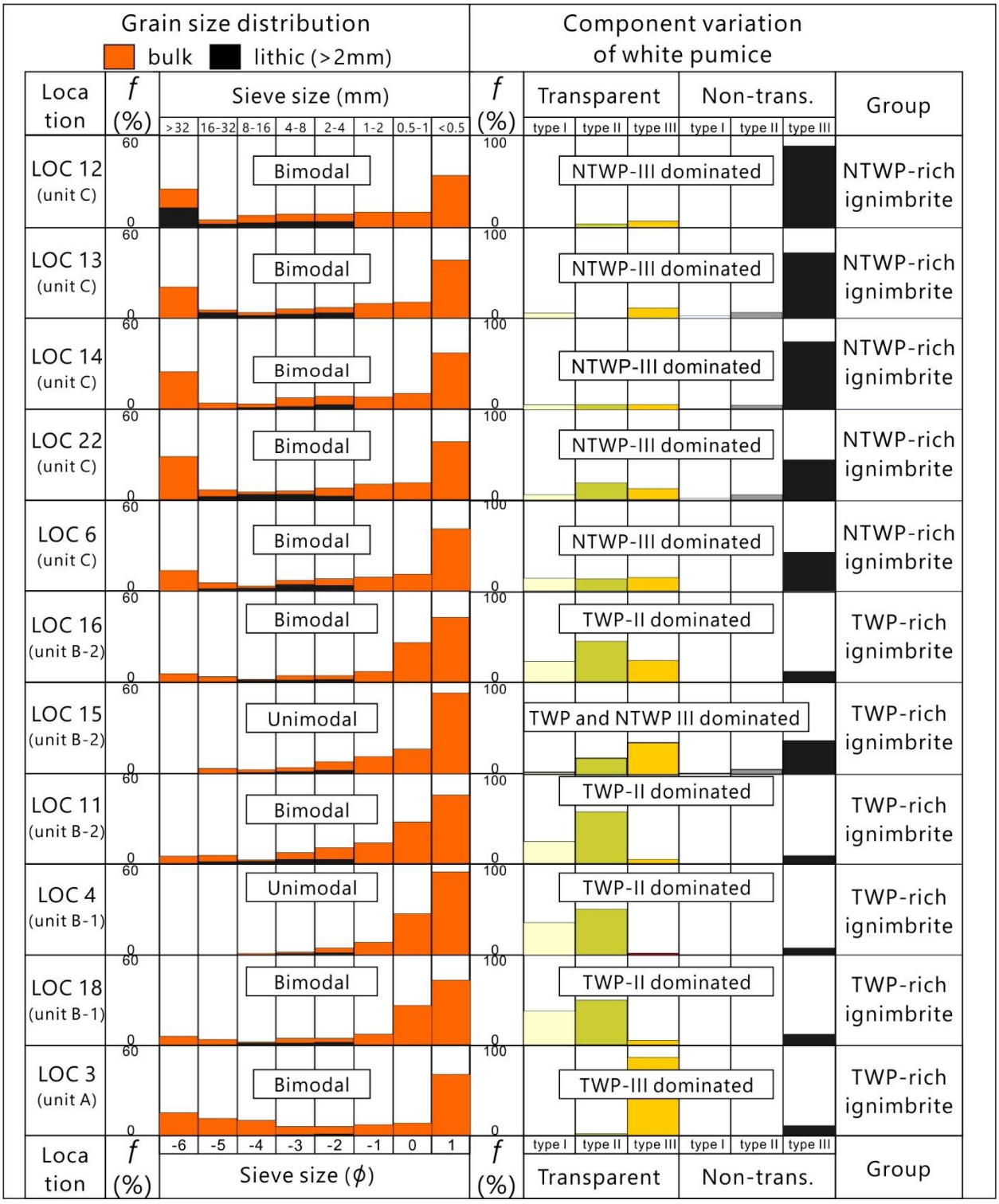

Figure 29. Correlation between the grain size distribution (GSD) data with component variation of white pumice types. There is tendency for type-III (elongated vesicle) pumices to produce higher portion of large grain particles, as it is more resistant toward fragmentation process than the pumices that are containing spherical vesicles.

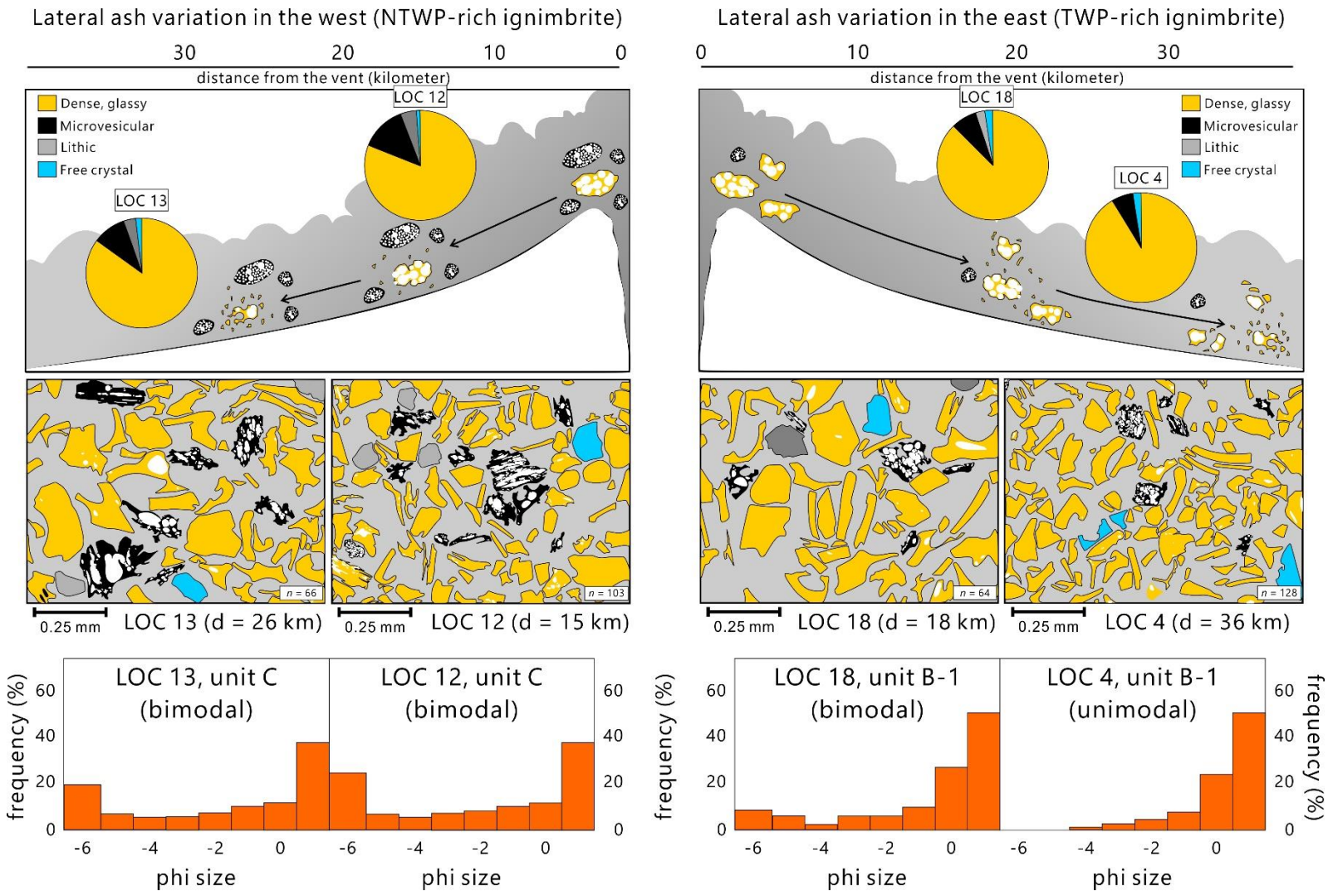

Figure 30. Cartoon showing the lateral variation of ash particles in the western (left image) and eastern deposits (right image). Western ignimbrite deposits have no lateral variation of ash particles due to the dominant portion of NTWP, hence is assumed to preserve its original GSD. By contrast, eastern ignimbrite show lateral variation of ash particles between the medial and distal facies (18 km and 36 km distance from the vent, respectively). The distal facies is characterized by a more abundant portion of the dense and glassy ash particles, which is presumed to be originated from the transparent white pumice.

7. Conclusion

This is the first study that report the occurrence of a highly unusual pumice type that we call ‘transparent’ pumice. Moreover, we also provide the first-detailed stratigraphic section of the 52 ka Maninjau caldera-forming eruption. Based on componentry data, we suggest that the stratigraphy of the 52 ka eruption can be divided as follows: Unit A, B-1, B-2, and C.

It is found that the transparent and non-transparent white pumice type have identical mineralogy and chemical compositions, suggesting that both types originated from the same (white) magma chamber. Based on our results, we argue that the transitions between TWP and NTWP strongly depends on the intensity of matrix-vesicle nucleation that controlled by magma decompression rate and the vertical variation of pheno-vesicle abundance in the pre-eruptive magma chamber. In short, it can be inferred that TWP originates from phenovesicle-dominated magma, while NTWP dose from phenovesicle-poor magma.

In addition, each pumice type (white, dark grey, pale grey, and light grey pumice) display distinctive mineralogy and chemical compositions. This strongly suggest that there were (at least) four different magma bodies beneath the Maninjau caldera. The white magma was stored in a relatively shallower crustal level compared to the grey magmas due to the absence of amphibole and the existence of quartz. Those of grey magmas were stored in different crustal levels with relatively similar temperature and water content.

We also interpret that such primary and secondary processes (represent as the difference in vesicle and pumice types, respectively) are likely responsible for the resultant grain size distribution data. In particular, an elongated vesicle-dominated magma tend to be more resistant toward fragmentation than spherical vesicle-dominated magmas, and subsequently, resulting in more abundant portion of large grains. Because TWP is typically fragile, an enrichment of fine-ash particles might occur during its transportation (syn-depositional) processes, yielding a relative decrease in large grains.

8. Acknowledgements

I would like to express my deepest gratitude to Dr. Atsushi Toramaru for his supervision, encouragement, guidance, and advices during my study, which significantly improves my scientific attitudes. I would like to thank to Dr. Takeshi Ikeda, Dr. Tomoharu Miyamoto, Kazuo Shimada from Kyushu University for the guidance in laboratory works,

criticism and advices. I am indebted to all of Petrology and Volcanology laboratory member for the togetherness, advices, and guidance in laboratory works.

Special gratitude to Volcano Special Education Scholarship for becoming my funding support during my study in Japan and Dr. Agung Harijoko and Dr. Haryo Edi Wibowo from Universitas Gadjah Mada (UGM) for his immeasurable help and support since I was undergraduate.

Sincere gratitude for my parents, Bapak Bambang Suhendro (father), Mama Magda Bhinnety Etsem, my brothers Indranu Suhendro and Indrasalva Suhendro, my sister Indrati Sudewi Suhendro, and all of my beloved friends for the endless support.

Many loves and many thanks to my wife, Awalina Aprilia Mitasari, and my son, Akira Nabeel Suhendro, for the love, support, and encouragement in every condition. Your unconditional support and love are very important for me.

9. References

Acocella, V., O. Bellier, L. Sandri, M. Sébrier, S. Pramumijoyo. 2018. Weak tectono-magmatic relationships along an obliquely convergent plate boundary: Sumatra, Indonesia. *Frontiers in Earth Science* 6.

Alloway, B.V., Pribadi, A., Westgate, J.A., Bird, M., Fifield, L.K., Hogg, A. & Smith, I. 2004. Correspondence between glass-FT and ^{14}C ages of silicic pyroclastic flow deposits sourced from Maninjau caldera, west-central Sumatra. *Earth and Planetary Science Letters* 227, pp. 121-133.

Allen, S.R. 2000. Reconstruction of a major caldera-forming eruption from pyroclastic deposit characteristics: Kos Plateau Tuff, eastern Aegean Sea. *Journal of Volcanology and Geothermal Research* 105, pp. 141 – 162.

Bellier, O., M. Sébrier 1994. Relationship between tectonism and volcanism along the Great Sumatran Fault Zone deduced by SPOT image analyses. *Tectonophysics* 233, pp. 215-231.

Chesner C.A., W.I. Rose. 1991. Stratigraphy of the Toba Tuffs and the evolution of the Toba Caldera Complex, Sumatra, Indonesia. *Bulletin of Volcanology* 53, pp. 343-356.

de Maisonneuve, C.B., O. Bachmann, A. Burgisser. 2009. Characterization of juvenile pyroclasts from the Kos Plateau Tuff (Aegean Arc): insights into the eruptive dynamics of a large rhyolitic eruption. *Bulletin of Volcanology* 71, pp. 643-658.

de Maisonneuve, C.B. and Bergal-Kuvikas, O. 2020. Timing, magnitude and geochemistry of major Southeast Asian volcanic eruptions: identifying tephrochronologic markers. *Journal of Quarternary Science* 35 (1-2), pp. 272-

287.

Druitt, T.H. and R.S.J. Sparks.1984. On the formation of calderas during ignimbrite eruptions. *Letters to Nature* 310, pp. 679-681.

Edmonds, M., and Woods, A.W. 2018. Exsolved volatiles in magma reservoirs. *Journal of Volcanology and Geothermal Research* 368, pp. 13-30.

Fernández-Blanco D., M. Philippon, C. von Hagke. 2016. Structure and kinematics of the Sumatran Fault system in North Sumatra (Indonesia). *Tectonophysics* 693, pp. 453-464.

Goff, F., R.G. Warren, C.J. Goff, N. Dunbar. 2014. Eruption of reverse-zoned upper Tshirege Member, Bandelier Tuff from centralized vents within Valles caldera, New Mexico. *Journal of Volcanology and Geothermal Research* 276, pp. 82-104.

Gurioli, L., B.F. Houghton, K.V., Cashman, R. Cioni. 2005. Complex changes in eruption dynamics during the 79 AD eruption of Vesuvius. *Bulletin of Volcanology* 67, pp. 144-159.

Harahap, B.H. and Abidin, Z.A. 2006. Petrology of lava from Maninjau lake, West Sumatra. *Journal of Geological Resource* 16:6, pp. 359-370.

Heiken, G., Wohletz, K., 1991. Fragmentation processes in explosive volcanic eruptions. *Sedimentation in Volcanic Settings* 45

Houghton, B.F., R.J. Carey, K.V. Cashman, C.J.N. Wilson, B.J. Hobden, J.E. Hammer. 2010. Diverse patterns of ascent, degassing, and eruption of rhyolite magma during the 1.8 ka Taupo eruption, New Zealand: Evidence from clast vesicularity. *Journal of Volcanology and Geothermal Research* 195, pp. 31-47.

Leo, G.W., Hedge, C.E. & Marvin, R.F. 1980. Geochemistry, strontium isotope data, and potassium-argon ages of the andesite-rhyolite association in the Padang area, West Sumatra. *Journal of Volcanology and Geothermal Research* 7, pp. 139-156.

Klug, C., K.V. Cashman. 1994. Vesiculation of May 18, 1980, Mount St. Helens magma. *Geology* 22, pp. 468-472.

Klug, C., K.V. Cashman. 1996. Permeability development in vesiculating magmas: implications for fragmentation. *Bulletin of Volcanology* 58, pp. 87-100.

Klug, C., K.V. Cashman, C.R. Bacon. 2002. Structure and physical characteristics of pumice from the climatic eruption of Mount Mazama (Crater Lake), Oregon. *Bulletin of Volcanology* 64, pp. 486-501.

Madden-Nadeau, A.L., M. Cassidy, D.M. Pyle, T.A. Mather, S.F.L. Watt, S.L. Engwell, M. Abdurrachman, M.E.M. Nurshal, D.R. Tappin, T. Ismail. 2020. The magmatic and eruptive evolution of the 1883 caldera-forming

eruption of Krakatau: Integrating field- to crystal-scale observations. *Journal of Volcanology and Geothermal Research* 411.

Maeno, F., H. Taniguchi. 2007. Spatiotemporal evolution of a marine caldera-forming eruption, generating a low-aspect ratio pyroclastic flow, 7.3 ka, Kikai caldera, Japan: Implication from near-vent eruptive deposits. *Journal of Volcanology and Geothermal Research* 167, pp. 212-238

Mertel, C., Dingwell., D.B., Spieler, O., Pichavant, M., Wilke, M., 2000. Fragmentation of foamed silicic melts: an experimental study. *Earth and Planetary Science Letters* 178, pp. 47-58

Mitchell, S.J., B.F. Houghton, R.J. Carey, M. Manga, K.E. Fauria, M.R. Jones, S.A. Soule, C. E. Conway, Z. Wei, T. Giachetti. 2019. Submarine giant pumice: a window into the shallow conduit dynamics of a recent silicic eruption. *Bulletin of Volcanology* 81:42

Natawidjadja, D.H., L. Bradley, M.R. Daryono, S. Aribowo, J. Herrin. 2017. Late quarternary eruption of the Ranau caldera and new geological slip rates of the Sumatran fault zone in southern Sumatra, Indonesia. *Geoscience Letters* 4:21

Polacci, M., P. Papale, M. Rosi. 2001. Textural heterogeneities in pumices from the climatic eruption of Mount Pinatubo, 15 June 1991, and implications for magma ascent dynamics. *Bulletin of Volcanology* 63, pp. 83-97.

Purbo-Hadiwidjoyo, M.M., Sjachrudin, M.L. & Suparka, S. 1979. The volcano-tectonic history of the Maninjau caldera, Western Sumatra, Indonesia. *Geol. Mijnbouw.* 58, pp. 193-200.

Reubi, O. and I.A. Nicholls. 2002. Variability in eruptive dynamics associated with caldera collapse: an example from two successive eruptions at Batur volcanic field, Bali, Indonesia. *Bulletin of Volcanology* 66, pp. 134-148.

Rose, W.I. and C.A. Chesner, 1994. Dispersal of ash in the great Toba eruption, 75 ka. *Geology* 15, pp. 913-917.

Rosi, M., L. Vezzoli, P. Aleotti, M.D. Censi. 1996. Interaction between caldera collapse and eruptive dynamics during the Campanian Ignimbrite eruption, Phlegraean Fields, Italy. *Bulletin of Volcanology* 57, pp. 541-554.

Salisbury, M.J., Patton, J.R., Kent, A.J.R., Goldfinger, C., Djadjadihardja, Y. & Hanifa, U. 2012. Deep-sea ash layers reveal evidence for large, late Pleistocene, and Holocene explosive activity from Sumatra, Indonesia. *Journal of Volcanology and Geothermal Research* 231-232, pp. 61-71.

Seggiaro, R.E., S.R. Guzmán, J. Martí. 2019. Dynamics of caldera collapse during the Coranzulí eruption (6.6 Ma) (Central Andes, Argentina). *Journal of Volcanology and Geothermal Research* 374, pp. 1-12.

Shea, T. 2017. Bubble nucleation in magmas: A dominantly heterogeneous process?. *Journal of Volcanology and Geothermal Research* 343, pp. 155-170.

Shea, T., Gurioli, L., B.F. Houghton. 2012. Transitions between fall phases and pyroclastic density currents during the AD 79 eruption at Vesuvius: building a transient conduit model from the textural and volatile record. *Bulletin of Volcanology* 74, pp. 2363-2381.

Sigurdsson, H., S. Carey. 1989. Plinian and co-ignimbrite tephra fall from the 1815 eruption of Tambora volcano. *Bulletin of Volcanology* 51, pp. 243-270.

Simmons, J.M., R.J. Carey, R.A.F. Cas, T.H. Druitt. 2017. High magma decompression rates at the peak of a violent caldera-forming eruption (Lower Pumice 1 eruption, Santorini, Greece). *Bulletin of Volcanology* 79:42.

Simmons, J.M., R.A.F. Cas, T.H. Druitt, C. Folkes. 2016. Complex variations during a caldera-forming Plinian eruption, including precursor deposits, thick pumice fallout, co-ignimbrite breccias and climatic lag breccias: The 184 ka Lower Pumice 1 eruption sequence, Santorini, Greece. *Journal of Volcanology and Geothermal Research* 324, pp. 200-219.

Suzuki-Kamata, K., H. Kamata, C.R. Bacon. 1993. Evolution of the caldera-forming eruption at Crater Lake, Oregon, indicated by component analysis of lithic fragments. *Journal of Geophysical Research* 98, pp. 14059-14074.

Toramaru, A. 2006. BND (bubble number density) decompression rate meter for explosive volcanic eruptions *Journal of Volcanology and Geothermal Research* 154, pp. 303-316.

Toramaru, A. 2014. On the second nucleation of bubbles in magmas under sudden decompression. *Earth and Planetary Science Letters* 404, pp. 190-199.

Wilson, L., R.S.J. Sparks, G.P.L. Walker. 1980. Explosivev volcanic eruptions – IV. The control of magma properties and conduit geometry on eruption column behaviour. *Gephysical Journal International Royal Astronomical Society* 63, pp. 117-148.

Vidal, C.M., N. Métrich., J.C. Komorowski, I. Pratomo, A. Michel, N. Kartadinata, V. Robert, F.Lavigne. 2015. Dynamics of the major plinian eruption of Samalas in 1257 A.D. (Lombok, Indonesia). *Bulletin of Volcanology* 77:73.

Vinci, A. 1985. Distribution and chemical composition of tephra layers from eastern Mediterranean abyssal sediments. *Marine Geology* 64, pp. 143-155.

Walker, G.P.L. 1971. Grain size characteristics of pyroclastic deposits. *The Journal of Geology* 79, pp. 696-714.

Table 1. Average glass compositions of all pumice types (normalized to 100 %)

Sample:	Transparent white pumice (TWP)	Non-transparent white pumice (NTWP)	Non-transparent dark grey pumice (from NTGP I and NTBP I)	Non-transparent pale grey pumice (from NTGP II and NTBP II)	Non-transparent light grey pumice (from NTBP III)
	n = 121	*n* = 111	*n = 30*	*n = 30*	*n = 30*
***wt* %**					
SiO_2	78.38	78.52	74.30	75.68	76.08
TiO_2	0.18	0.18	0.368	0.27	0.20
Al_2O_3	13.13	12.8	15.09	14.45	13.91
MnO	0.11	0.11	0.08	0.06	0.05
MgO	0.10	0.10	0.71	0.46	0.35
CaO	0.78	0.79	2.43	1.95	1.59
Na_2O	2.10	2.10	2.24	2.25	2.62
K_2O	4.60	4.60	2.43	3.11	3.74
FeO	0.62	0.60	2.05	1.48	1.29
Total	99.9	99.99	99.9	99.9	99.9

Table 2. Textural parameter of transparent white pumice

Location, unit, pumice type	Bulk density (gr/cm^3)	Bulk vesicularity (%)	Pheno-vesicle			Matrix-vesicle			Phenocryst Content (%)
			Average diameter (mm)	Fraction (%)	Nv (m^{-3})	Average diameter (mm)	Fraction (%)	Nv (mm^{-3})	
2 (E), unit 1 TWP II	0.83	60.5	0.30	56.5	$1.8x10^{11}$	0.04	4.0	$7.5x10^{11}$	0
	0.60	70.5	0.27	54.9	$1.6x10^{11}$	0.035	6.6	$1.3x10^{12}$	7.9
	0.56	75.3	0.28	70.0	$1.4x10^{11}$	0.037	5.3	$1.4x10^{12}$	18.2
2 (E), unit 1 TWP III	1.12	48.2	0.23	42.6	$1.2x10^{11}$	0.022	12.4	$5.8x10^{13}$	0
	0.92	58.1	0.24	61.6	$2.0x10^{11}$	0.035	8.4	$1.8x10^{13}$	21.0
	0.77	67.0	0.23	45.6	$1.4x10^{11}$	0.021	29.4	$2.0x10^{14}$	23.6

16 (N), unit 2	0.84	62.0	0.29	58.2	$1.9x10^{11}$	0.039	3.8	$7.8x10^{11}$	0
TWP I	0.56	76.0	0.30	71.0	$1.8x10^{11}$	0.041	5.0	$6.9x10^{11}$	0
	0.46	80.3	0.30	76.5	$2.5x10^{11}$	0.042	4.5	$5.2x10^{11}$	0
16 (N), unit 2	1.07	51.0	0.29	48.0	$1.8x10^{11}$	0.039	3.0	$7.0x10^{11}$	0
TWP III	0.77	61.1	0.22	48.4	$1.8x10^{11}$	0.025	15.6	$4.3x10^{13}$	8.0
	0.66	68.0	0.26	62.0	$2.5x10^{11}$	0.031	8.0	$1.0x10^{12}$	0
11 (E), unit 3	0.75	69.6	0.32	73.8	$2.0x10^{11}$	0.042	4.3	$4.9x10^{11}$	0
TWP II	0.55	75.1	0.30	77.0	$2.5x10^{11}$	0.042	5.0	$8.2x10^{11}$	0
	0.42	81.9	0.31	73.0	$1.4x10^{11}$	0.040	9.0	$1.2x10^{12}$	0
11 (E), unit 3	1.06	52.0	0.28	48.5	$1.6x10^{11}$	0.038	3.5	$6.8x10^{11}$	0
TWP III	0.86	62.1	0.25	62.0	$1.9x10^{11}$	0.031	3.1	$1.1x10^{12}$	0
	0.61	70.3	0.26	56.6	$1.4x10^{11}$	0.025	13.7	$4.1x10^{13}$	0
15 (N), unit 3	0.82	58.4	0.18	38.3	$1.8x10^{11}$	0.009	20.1	$8.2x10^{14}$	0
TWP II	0.67	64.2	0.21	47.2	$1.8x10^{11}$	0.028	17.0	$6.0x10^{12}$	0
	0.6	70.0	0.28	64.8	$1.9x10^{11}$	0.028	5.2	$2.3x10^{12}$	0
15 (N), unit 3	1.08	50.6	0.17	24.5	$1.3x10^{11}$	0.006	21.5	$1.7x10^{15}$	0
TWP III	0.74	63.7	0.19	33.1	$1.5x10^{11}$	0.016	30.6	$2.3x10^{14}$	4.3
	0.65	66.0	0.21	36.2	$1.5x10^{11}$	0.023	29.8	$4.3x10^{13}$	0.2
22 (S), unit 4	0.74	68.0	0.28	24.5	$1.3x10^{11}$	0.039	5.0	$9.6x10^{11}$	11.3
TWP I	0.57	75.0	0.30	33.1	$1.5x10^{11}$	0.040	5.0	$8.5x10^{11}$	30.6
	0.40	83.0	0.34	36.2	$1.5x10^{11}$	0.040	8.3	$1.3x10^{12}$	0
22 (S), unit 4	0.79	62.0	0.29	65.0	$1.3x10^{11}$	0.027	8.0	$6.1x10^{12}$	2.3
TWP II	0.49	78.5	0.28	62.3	$1.4x10^{11}$	0.029	16.2	$1.1x10^{13}$	8.3
	0.47	81.5	0.32	72.3	$1.5x10^{11}$	0.036	9.2	$1.1x10^{12}$	0
22 (S), unit 4	1.18	48.9	0.17	28.2	$1.5x10^{11}$	0.005	20.7	$2.9x10^{15}$	0.5
TWP III	0.75	63.7	0.21	43.8	$1.6x10^{11}$	0.020	19.9	$6.4x10^{13}$	1.2
	0.68	68.0	0.23	59.4	$1.8x10^{11}$	0.021	8.6	$3.0x10^{13}$	5.2
12 (W), unit 4	0.94	54.9	0.19	33.5	$1.3x10^{11}$	0.006	21.4	$4.3x10^{15}$	0.6
TWP III	0.62	67.0	0.26	59.6	$1.4x10^{11}$	0.023	7.4	$7.2x10^{13}$	2.5
	0.49	75.0	0.23	54.3	$1.6x10^{11}$	0.035	12.8	$2.5x10^{13}$	0
	0.81	62.0	0.23	58.2	$1.8x10^{11}$	0.033	3.8	$3.5x10^{12}$	0

13 (W), unit 4 TWP II	0.57	70.1	0.25	49.8	$1.4x10^{11}$	0.021	20.2	$9.8x10^{13}$	0
	0.41	83.0	0.32	79.2	$2.1x10^{11}$	0.037	5.8	$1.5x10^{12}$	0
13 (W), unit 4 TWP III	0.97	55.1	0.23	47.4	$1.1x10^{11}$	0.015	7.7	$4.0x10^{14}$	0
	0.67	68.0	0.23	51.7	$1.7x10^{11}$	0.019	16.3	$9.0x10^{13}$	0
	0.58	71.0	0.25	68.2	$1.8x10^{11}$	0.036	6.8	$1.4x10^{13}$	1.3
14 (W), unit 4 TWP III	0.82	59.0	0.21	43.9	$1.6x10^{11}$	0.028	15.1	$3.5x10^{13}$	0
	0.67	65.3	0.19	41.3	$1.7x10^{11}$	0.020	23.7	$1.1x10^{14}$	0
	0.40	80.5	0.29	62.0	$1.6x10^{11}$	0.042	18.0	$1.2x10^{12}$	0

Table 3. Textural parameter of non-transparent white pumice

Location, unit, pumice type	Bulk density (gr/cm^3)	Bulk vesicularity (%)	Pheno-vesicle			Matrix-vesicle			Phenocryst Content (%)
			Average diameter (mm)	Fraction (%)	Nv (m^{-3})	Average diameter (mm)	Fraction (%)	Nv (mm^{-3})	
2 (E), unit 1 NTWPIII	1.01	54.7	0.19	24.3	$9.9x10^{10}$	0.0035	30.4	$1.3x10^{16}$	27.3
	0.83	61.5	0.20	21.5	$8.7x10^{10}$	0.0036	40.0	$2.0x10^{16}$	1.5
	0.71	68.0	0.18	28.1	$1.3x10^{10}$	0.0044	39.9	$1.1x10^{16}$	2.2
16 (N), unit 2 NTWPIII	0.92	56.9	0.17	26.8	$1.7x10^{11}$	0.0038	28.1	$9.7x10^{15}$	3.9
	0.87	61.0	0.16	17.1	$1.3x10^{11}$	0.0039	47.9	$1.6x10^{16}$	0
	0.66	67.0	0.19	31.5	$1.6x10^{11}$	0.0039	35.5	$6.6x10^{15}$	0.2
17 (N), unit 2 NTWPIII	0.92	58.0	0.18	24.1	$1.2x10^{11}$	0.0044	33.9	$1.1x10^{16}$	5.1
	0.77	60.1	0.18	18.7	$1.0x10^{11}$	0.0033	41.4	$2.2x10^{16}$	0
	0.59	70.3	0.19	22.7	$1.6x10^{11}$	0.0053	47.6	$7.6x10^{15}$	0
11 (E), unit 3 NTWPIII	0.90	59.8	0.15	8.4	$7.4x10^{10}$	0.0038	51.4	$2.7x10^{16}$	0
	0.79	64.9	0.15	15.2	$1.4x10^{11}$	0.0040	49.7	$1.8x10^{16}$	0
	0.61	67.0	0.19	25.7	$1.6x10^{11}$	0.0041	41.3	$1.5x10^{16}$	0
15 (N), unit 3 NTWPIII	0.92	54.3	0.17	11.7	$8.3x10^{10}$	0.0040	42.6	$2.1x10^{16}$	0
	0.79	61.0	0.19	11.3	$5.5x10^{10}$	0.0040	49.7	$2.6x10^{16}$	6.2
	0.58	71.4	0.17	13.7	$1.2x10^{11}$	0.0043	57.7	$1.5x10^{16}$	0
6 (E), unit 4 NTWPIII	0.96	55.0	0.23	26.0	$5.9x10^{10}$	0.0029	29.0	$2.1x10^{16}$	4.6
	0.81	63.0	0.20	8.7	$3.5x10^{10}$	0.0032	54.3	$2.8x10^{16}$	2.1
	0.63	67.4	0.21	18.5	$7.8x10^{10}$	0.0033	48.5	$1.6x10^{16}$	0
22 (S), unit 4 NTWPI	0.48	75.0	0.17	13.1	$1.2x10^{11}$	0.0051	57.9	$1.0x10^{16}$	12.3
	0.39	82.6	0.22	30.2	$1.7x10^{11}$	0.0045	52.4	$1.2x10^{16}$	6.1
	0.29	87.9	0.22	23.0	$1.8x10^{11}$	0.0054	64.9	$1.1x10^{16}$	3.8
22 (S), unit 4 NTWPII	0.82	59.7	0.20	19.9	$8.4x10^{10}$	0.0044	39.8	$1.8x10^{16}$	0
	0.65	65.0	0.19	11.4	$6.4x10^{10}$	0.0062	53.6	$1.5x10^{16}$	0.8
	0.59	69.0	0.22	18.3	$7.4x10^{10}$	0.0058	50.7	$1.4x10^{16}$	9.6
22 (S), unit 4 NTWPIII	0.91	54.5	0.18	9.1	$4.6x10^{10}$	0.0031	45.4	$3.4x10^{16}$	4.6
	0.72	64.0	0.19	14.1	$7.4x10^{10}$	0.0031	49.9	$3.7x10^{16}$	2.2
	0.68	69.0	0.18	12.5	$9.0x10^{10}$	0.0034	56.5	$3.6x10^{16}$	2.2

12 (W), unit 4 NTWPIII	0.97	54.1	0.18	15.9	$7.1x10^{10}$	0.0028	38.2	$3.2x10^{16}$	7.4
	0.68	63.0	0.17	10.8	$6.8x10^{10}$	0.0025	52.2	$8.2x10^{16}$	15.8
	0.57	69.0	0.17	18.9	$1.6x10^{11}$	0.0041	50.1	$2.2x10^{16}$	16.6
13 (W), unit 4 NTWPIII	0.93	58.4	0.13	4.6	$5.2x10^{10}$	0.0025	53.8	$8.9x10^{16}$	0
	0.72	62.0	0.14	12.6	$1.5x10^{11}$	0.0036	49.4	$2.5x10^{16}$	0
	0.58	72.0	0.17	19.0	$1.5x10^{11}$	0.0036	51.0	$2.5x10^{16}$	1.5
14 (W), unit 4 NTWPII	0.87	59.6	0.18	13.4	$1.2x10^{11}$	0.0053	46.2	$6.2x10^{15}$	0
	0.64	67.0	0.19	14.6	$8.2x10^{10}$	0.0056	51.6	$7.2x10^{15}$	0
	0.51	73.0	0.20	21.4	$1.2x10^{11}$	0.0058	55.6	$6.0x10^{15}$	2.0
14 (W), unit 4 NTWPIII	0.98	52.3	0.18	21.5	$1.0x10^{11}$	0.0028	30.5	$2.6x10^{16}$	6.5
	0.63	66.0	0.18	19.2	$1.3x10^{11}$	0.0035	48.3	$1.8x10^{16}$	0
	0.57	70.1	0.19	28.4	$1.6x10^{11}$	0.0042	41.6	$1.3x10^{16}$	0

Table 4. Textural parameter of non-transparent grey pumices

Location, unit, pumice type	Bulk density (gr/cm^3)	Bulk vesicularity (%)	Pheno-vesicle			Matrix-vesicle			Phenocryst Content (%)
			Average diameter (mm)	Fraction (%)	Nv (m^{-3})	Average diameter (mm)	Fraction (%)	Nv (mm^{-3})	
6 (E), unit 4 NTGP I	0.75	71.3	0.26	9.3	$2.4x10^{10}$	0.0033	62.0	$3.6x10^{16}$	39.7
	0.66	75.9	0.26	12.5	$3.6x10^{10}$	0.0040	63.4	$3.4x10^{16}$	72.4
	0.52	79.6	0.28	12.7	$3.7x10^{10}$	0.0034	66.8	$2.2x10^{16}$	52.0
12 (W), unit 4 NTGP I	1.17	53.3	0.27	17.3	$2.4x10^{10}$	0.0038	36.0	$3.1x10^{16}$	30.1
14 (W), unit 4 NTGP I	0.60	74.8	0.26	13.9	$4.2x10^{10}$	0.0037	60.9	$1.6x10^{16}$	27.8
	0.56	78.7	0.27	13.7	$4.0x10^{10}$	0.0040	65.0	$1.8x10^{16}$	39.5
	0.43	81.4	0.26	7.3	$5.3x10^{10}$	0.0036	74.1	$1.3x10^{16}$	62.2
6 (E), unit 4 NTGP II	0.68	73.7	0.24	37.7	$1.9x10^{11}$	0.0051	40.0	$9.6x10^{15}$	16.9
	0.39	83.0	0.29	38.0	$1.9x10^{11}$	0.0057	45.0	$6.9x10^{15}$	2.9
	0.23	91.5	0.30	39.0	$2.3x10^{11}$	0.0067	52.5	$6.9x10^{15}$	87.0
12 (W), unit 4 NTGP II	0.80	72.1	0.28	32.1	$4.3x10^{10}$	0.0030	40.0	$4.0x10^{16}$	11.3

14 (W), unit 4 NTGP II	0.90	70.9	0.24	29.6	$1.3x10^{11}$	0.0074	41.3	$7.8x10^{15}$	25.7
	0.79	78.4	0.21	22.1	$1.6x10^{11}$	0.0070	56.3	$5.1x10^{15}$	9.1
	0.61	81.4	0.16	10.2	$1.6x10^{11}$	0.0065	71.2	$1.1x10^{16}$	78.0
22 (S), unit 4 NTBP III	-	75.8	0.26	14.3	$3.0x10^{10}$	0.0024	61.5	$6.0x10^{16}$	60.1